

Aleksi Vesterinen

CONCEPTUAL DESIGN OF AN ELECTRIC FOUR DEGREES OF FREEDOM MOBILE MANIPULATOR

Master of Science Thesis
Faculty of Engineering and Natural Sciences
Examiners: Prof. Jouni Mattila
M.Sc Goran Petrović
May 2022

ABSTRACT

Aleksi Vesterinen: Conceptual design of an electric four degrees of freedom mobile manipulator

Master of Science Thesis

Tampere University

Master's Degree Program in Mechanical Engineering

May 2022

Mobile machinery has been moving towards more autonomous solutions to remove workers from hazardous areas and relocate them to places where work can be done safely. This has driven companies to develop machinery that can be controlled remotely. These machines are designed to do the jobs that people have carried out in the past in dangerous areas. At the same time, the world is electrifying due to legislation and environmental awareness. Hydraulic actuators have long dominated the market in the production of linear motion. Today's emissions regulations as well as environmental awareness have driven companies to think about new approaches to reduce emissions and replace the oil used in machinery. Electromechanical linear actuators (EMLAs) are designed to replace hydraulic cylinders. These days EMLAs can produce forces that are suitable to replace hydraulic cylinders in many applications.

This thesis utilizes theory and simulations to explain what to consider when designing a mobile manipulator with EMLAs. The paper presents the differences between hydraulic cylinders and EMLAs and how these differences are reflected in the behavior of the mobile manipulator's arm under study. The work also reviews current industrial robots and mobile manipulators and evaluates their suitability for different environments and work tasks. The most important criterion in the design of a mobile manipulator is not only the forces that actuators can provide but also the stability of the mobile manipulator which limits the lifting capacity. Therefore, the lifting capacity of the actuators and the prevention of the mobile manipulator from overturning are things that need to be designed in parallel.

The results of the thesis show that simulation is powerful tool for dimensioning EMLAs and gather information on the forces and velocities acting the actuators. Simulation can be used to design the manipulator and test the whole device and consider the stability at the same time. Simulation or analytic calculations allows to study the natural frequencies of the manipulator and to compare hydraulic cylinders and EMLAs. The results show that with EMLAs it is possible to improve the dynamics of the manipulator compared to hydraulic cylinders because the stiffness of hydraulic cylinder is many times lower than that of the corresponding EMLA.

Keywords: Mobile manipulator, hydraulic cylinder, EMLA, natural frequency, simulation

The originality of this thesis has been checked using the Turnitin OriginalityCheck service.

TIIVISTELMÄ

Alexi Vesterinen: Sähkökäyttöisen neljän vapausasteen mobiilimanipulaattorin konseptisunnittelu

Diplomityö

Tampereen yliopisto

Konetekniikan diplomi-insinööri koulutusohjelma

Toukokuu 2022

Liikkuvat työkoneet ovat muuttuneet koko ajan autonomisempaan suuntaan, jotta työntekijät saataisiin pois vaarallisilta alueilta ja siirrettyä paikkoihin, joissa työ voidaan tehdä turvallisesti. Tämä on ajanut ihmiset kehittämään laitteita, joita voidaan ohjata etänä. Laitteet mahdollistavat työtehtävien teon, joita ihmiset ennen tekivät vaarallisilla alueilla. Samaan aikaan maailma on sähköistymässä lainsäädännön sekä ympäristötietoisuuden vuoksi. Hydrauliset toimilaitteet ovat hallinneet pitkään markkinoita lineaariliikkeen tuottamisessa. Nykypäivän päästö määräykset sekä ympäristötietoisuus ovat ajaneet yritykset miettimään uusia lähestymistapoja päästöjen vähentämiseen ja laitteissa olevan öljyn poistamiseen. Sähkösylinterit ovat suunniteltu korvaamaan hydraulisyylinterit. Nykyään sähkösylinterit pystyvät tuottamaan voimia, jotka sopivat hydraulisyylinterien korvaamiseksi monessa sovelluksessa.

Tämä opinnäytetyö selittää teorian ja simulointien avulla, mitä pitää ottaa huomioon, kun suunnitellaan mobiilimanipulaattoria sähkösylintereillä. Työssä esitetään hydraulisyylinterien ja sähkösylinterien eroja sekä kuinka nämä erot näkyvät tutkittavan manipulaattorin käyttäytymisessä. Työssä myös käydään läpi tämänhetkisiä teollisuusrobotteja sekä mobiilimanipulaattoreita ja arvioidaan näiden soveltuvuutta erilaisiin ympäristöihin ja työtehtäviin. Mobiilimanipulaattorin suunnittelussa tärkein kriteeri ei ole aina manipulaattorin voiman tuotto, vaan rajoitteena on myös laitteen stabiiliteetti, joka rajoittaa nostettavien kuormien suuruuksia. Näin ollen toimilaitteiden nostokyky sekä laitteen kaatumisen estäminen ovat asioita, jotka pitää suunnitella rinnakkain.

Tämän opinnäytetyön tulokset osoittavat, että simulointi on hyvä työkalu sähkösylinterien mitoittamiseen ja toimilaitteisiin kohdistuvien voimien ja nopeuksien selvittämiseen. Simulaattorilla voidaan suunnitella manipulaattori tai koko laite ja huomioida myös sen stabiilisuus. Simulointi tai analyttiset laskelmat mahdollistavat manipulaattorin ominaistuuksien tutkimisen sekä hydraulisyylinterien ja sähkösylinterien vertailemisen. Tulokset kertovat, että sähkösylintereillä on mahdollista saada manipulaattori dynamiikka paremmaksi verrattuna hydraulisyylintereihin, joiden jäykkyydet ovat monikerroin pienemmät kuin sähkösylinterien jäykkyydet.

Avainsanat: Mobiilimanipulaattori, hydraulisyylinteri, sähkösylinteri, ominaistuuksisuus, simulointi

Tämän julkaisun alkuperäisyys on tarkastettu Turnitin OriginalityCheck –ohjelmalla.

PREFACE

I would like to thank my great friends who have always been helpful and supportive during my studies. My thanks also go to Jouni Mattila and Goran Petrovic for the guidance and assistance I have received during this process. I would like to express my gratitude to my family who have supported me from the beginning of my studies to this point. Finally, and especially, thanks go to my fiancée Jasmiina for the support throughout these years.

Tampere, 21 May 2022

Aleksi Vesterinen

CONTENTS

1.INTRODUCTION	1
1.1 Background.....	1
1.2 Objectives of the thesis	2
1.3 Structure of the thesis	2
2.HYDRAULIC AND ELECTRIC ACTUATORS	4
2.1 Hydraulic cylinders.....	5
2.1.1 Hydraulic cylinder basic equations	7
2.1.2 Stiffness of hydraulic cylinder.....	7
2.1.3 Inertia of hydraulic cylinder	8
2.1.4 Natural frequency with hydraulic cylinder	9
2.2 Electromechanical linear actuators.....	10
2.2.1 Screw types	11
2.2.2 Sizing of EMLA	13
2.2.3 Stiffness of EMLA	16
2.2.4 Inertia of EMLA	23
2.2.5 Natural frequencies of EMLA	25
3.ROBOTS.....	26
3.1 High payload industrial robots	27
3.2 Limitations of industrial robots in mobile applications	28
3.3 Mobile manipulators.....	29
4.MOBILE MANIPULATOR STABILITY MONITORING	32
4.1 Reaction forces	32
4.2 Stability margins and tipping angles	35
5.SIMULATION RESULTS.....	36
5.1 Manipulator's actuator forces and velocities	37
5.2 Manipulator's natural frequencies.....	39
5.3 Stability of the mobile manipulator.....	44
6.CONCLUSIONS.....	45
REFERENCES.....	47
APPENDIX A: LENGTH OF THE ACTUATORS AND JOINT ANGLES.....	52
APPENDIX B: DH-PARAMETERS	55
APPENDIX C: FORWARD KINEMATICS.....	56
APPENDIX D: SIMULATION MODEL	57

LIST OF FIGURES

Figure 1.	<i>The first patent of EMLA and the first modern EMLA. [10], [11]</i>	4
Figure 2.	<i>Simple hydraulic schematic.</i>	5
Figure 3.	<i>Simplified structure of a single-acting cylinder.</i>	6
Figure 4.	<i>Simplified structure of a double-acting hydraulic cylinder.</i>	6
Figure 5.	<i>Components of EMLA.</i>	10
Figure 6.	<i>Ball screw, lead screw and roller screw. [16]–[18]</i>	11
Figure 7.	<i>Process for sizing a screw system.</i>	13
Figure 8.	<i>Buckling loads and effective lengths. [29].</i>	15
Figure 9.	<i>Stiffness components of EMLA.</i>	17
Figure 10.	<i>Ball screw design parameters. [33]</i>	18
Figure 11.	<i>Inertial components of EMLA.</i>	23
Figure 12.	<i>2-DOF mechanical model. [41].</i>	25
Figure 13.	<i>Pictures of SHAKEY and Lunokhod-1. [47], [48]</i>	27
Figure 14.	<i>ABB IRB8700, Fanuc M-2000ia/2300 and KUKA KR1000 titan. [52]–[54].</i>	28
Figure 15.	<i>KUKA KMR QUANTEC. [57]</i>	30
Figure 16.	<i>L3Harris T7 and Telerob tEODor EVO. [59], [60]</i>	30
Figure 17.	<i>LUGV. [61]</i>	31
Figure 18.	<i>Graphical presentation of the CSP and SP.</i>	34
Figure 19.	<i>Reference end-effector path and simulated path.</i>	36
Figure 20.	<i>Position reference, measured position and maximum error for all joints.</i>	37
Figure 21.	<i>Actuator forces, velocities and powers of the EMLAs.</i>	38
Figure 22.	<i>Natural frequencies of the manipulator.</i>	40
Figure 23.	<i>Manipulator posture and oscillation directions.</i>	41
Figure 24.	<i>Natural frequencies of the hydraulic cylinder and EMLA in 1-DOF case.</i>	43
Figure 25.	<i>Reaction forces for four wheels.</i>	44

ABBREVIATIONS

ICE	Internal combustion engine
NRMM	Non-road mobile machinery
NO _x	Oxides of nitrogen
HC	Hydrocarbons
CO ₂	Carbon dioxide
PM	Particulate matter
GHG	Greenhouse gas
FCEV	Fuel cell electric vehicle
PHEV	Plug-in hybrid vehicle
BEV	Battery electric vehicle
EHA	Electro-hydraulic actuator
EMLA	Electro-mechanical linear actuator
MM	Mobile manipulator
CoG	Center of gravity
PSD	Power spectral density
ZMP	Zero-Moment Point
FA	Force-Angle
MHS	Moment-Height Stability

1. INTRODUCTION

The primary power source for mobile machinery is an internal combustion engine (ICE) powered by diesel [1]. Commonly, mobile machinery uses a hydraulic system to transfer the energy from ICE to hydraulic linear actuators or motors via fluid power transmission lines. However, the electrification of machinery is a huge trend due to the regulations, legislation, and awareness of climate change. The non-road mobile machinery (NRMM) causes an emission of nitrogen oxides (NO_x), hydrocarbons (HC), particulate matter (PM) and carbon dioxide (CO₂), among others. The carbon oxide has the most impact on the global warming. The NRMM accounts for about 11 % of the greenhouse gas (GHG) emissions of that of road transport in Europe.[2] The alternative options for the traditional hydraulic and mechanical powertrains are electric powertrains which do not necessary need hydraulic oil as an energy carrier between power source and actuators.

1.1 Background

Electric powertrains have gained popularity in the automobile industry and the growth rates have been significant. In 2020, electric cars represented 10 % of the registered cars in Europe. Electric cars include fuel cell electric vehicles (FCEV), plug-in hybrid electric vehicles (PHEV) and battery electric vehicles (BEV) [3]. The electrification growth in the mobile machinery industry has not been as fast as in automobile industry. However, some pioneer manufacturers have developed electric NRMM. For example, manufacturers such as Volvo and Yanmar, have developed full-electric excavators powered by batteries. Volvo's excavator uses electro-hydraulic actuators (EHA) and Yanmar's excavator uses electro-mechanical linear actuators (EMLA) for the movements of the arm [4], [5]. Yanmar's excavator can be referred to as all-electric NRMM as there is no hydraulic fluid in the system. These machines are smaller than the most popular excavators, but the technology is developing. One big step towards NRMM electrification happened in January 2022 when BOBCAT introduced the production version of all-electric skid-steer loader T7X which has higher capabilities compared than similar hydraulic loader. The performance of the T7X comes from EMLAs with ball screw actuators and high torque traction motors which have three times higher torque output compared to hydraulic loader. [6]

Electrification in the mobile machinery industry makes it possible to improve safety in new ways. Traditionally, mobile machinery is controlled from inside a cabin but nowadays controlling the machines can be done remotely via different communication methods. This allows the mobile machine industry to deliver more autonomous solutions for use in dangerous environments. As a result, there exist different machines e.g., demolition robots, excavators and mining machines that can be controlled remotely from safer areas. In addition to remotely controlled vehicles, there have been developed autonomous systems such as autonomous excavator system for digging and material loading tasks [7] and autonomous loader for mining [8]. As humans are moved to safer environments, these machines need assistance from smaller mobile manipulators which execute the tasks that larger machines are not able to perform.

1.2 Objectives of the thesis

In this thesis, a conceptual design for an electric four degrees of freedom manipulator arm for mobile manipulator (MM) is presented. The thesis develops an overview of what needs to be considered when designing a fully electric manipulator with EMLAs and how to prevent the MM from overturning. The MM concept is different from existing MMs that are often integrated by combination of a mobile robot and industrial robot. Industrial robot's bulky rigid structure link joints are usually driven by motors and gearboxes. In this concept, the manipulator structure consists of welded steel structure links which enables high (over 1:1) payload to weight ratios. The first objective is to compare hydraulic cylinders and EMLAs and to present their differences. The second objective is to represent the state-of-the-art industrial robots and mobile manipulators and discuss their capabilities. The overturning stability of the MM is essential; therefore, one objective is to describe a way to prevent the tip-over of the MM. Finally, simulation model for the MM with EMLAs is presented and a comparison of natural frequencies between the hydraulic cylinder and the EMLA is performed.

1.3 Structure of the thesis

This thesis is divided into five chapters and four appendices. Chapter 2 contains the comparison between hydraulic actuators and EMLAs. The chapter reviews the operating principles and the properties of hydraulic cylinders and EMLAs. In Chapter 3, the suitability of industrial robots for mobile applications is reviewed and the properties of the state-of-the-art industrial robots and mobile manipulators are discussed. Chapter 4 presents a method to calculate the reaction forces between the ground and wheels of a

structure with an arbitrary number of ground contacts. Chapter 5 presents the dimensioning of EMLAs using methods from Chapter 2 and the comparison of the natural frequencies between the hydraulic cylinder and EMLA. The last chapter summarizes the key findings, discusses the limitations of the study, and provides ideas for future work. Appendix A presents the calculation of the actuator lengths from the joint angles. Appendix B presents forming the Denavit-Hartenberg (DH) parameters for MM. Appendix C gives the methods to calculate the forward kinematics. Appendix D describes the simulation model for the mobile manipulator.

2. HYDRAULIC AND ELECTRIC ACTUATORS

The history of fluid power dates back thousands of years. However, the first scientific studies were made in the 17th century when Blaise Pascal noticed that the pressure in a fluid is equally distributed in all directions [9]. For decades, hydraulic systems have been the main power transfer systems in heavy-duty applications where high power and forces are required. One of the main components of a hydraulic system is a hydraulic cylinder which is used in many applications in different industries. An electrical alternative for a hydraulic cylinder is an electromechanical linear actuator. It is relatively rarely used in linear motion applications compared to hydraulic cylinders, especially in mobile machinery. The first electric actuator dates back to 1945, when Howard M. McCoy patented an electric jack related to the control of airplane propellers [10]. However, the first modern EMLA, named LA30, was invented in the late 1970s by Danish engineer Bent Jensen from the company Christian Jensen & Sons. The EMLA was used primarily in agricultural applications. [11] Nowadays, the company has changed its name to LINAK, and it manufactures EMLAs for different applications. The structures of the EMLAs are different, as shown in Figure 1.

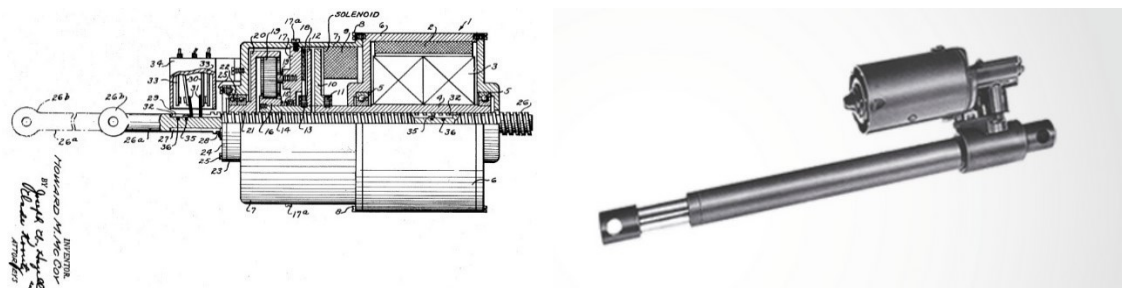


Figure 1. The first patent of EMLA and the first modern EMLA. [10], [11]

This chapter discusses the differences between the hydraulic cylinder and EMLA. In Section 2.1, the operating principle of a hydraulic cylinder is presented and along with formulas to evaluate basic properties like the stiffness of the cylinder and natural frequencies. Section 2.2 discusses the properties of EMLAs and the properties of different screw types. In addition, the formulas to calculate the stiffness and natural frequency of EMLAs are presented.

2.1 Hydraulic cylinders

A hydraulic cylinder is a component in a hydraulic system that converts the fluid power into mechanical linear motion. The fluid power is usually provided by the rotational motion of an engine or an electric motor. The power is transferred to hydraulic motors or hydraulic cylinders via hydraulic fluid and the motion is controlled with valves. A simple hydraulic schematic with common hydraulic components is shown in Figure 2.

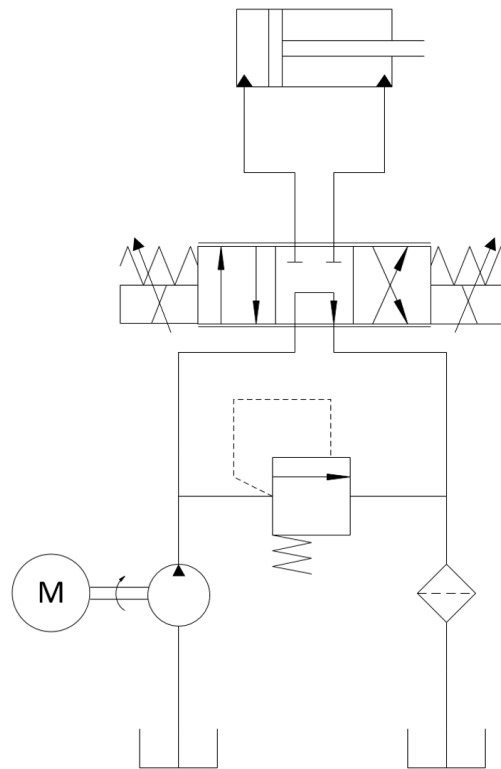


Figure 2. Simple hydraulic schematic.

Hydraulic cylinders can be divided into two single-acting cylinders and double-acting cylinders. They are both used in different applications. Single-acting cylinders are used in applications where high forces are not needed in both directions. These kinds of applications are e.g., brakes, fasteners and lifting pallets. [12] A piston-type single-acting cylinder with spring return is shown in Figure 3.

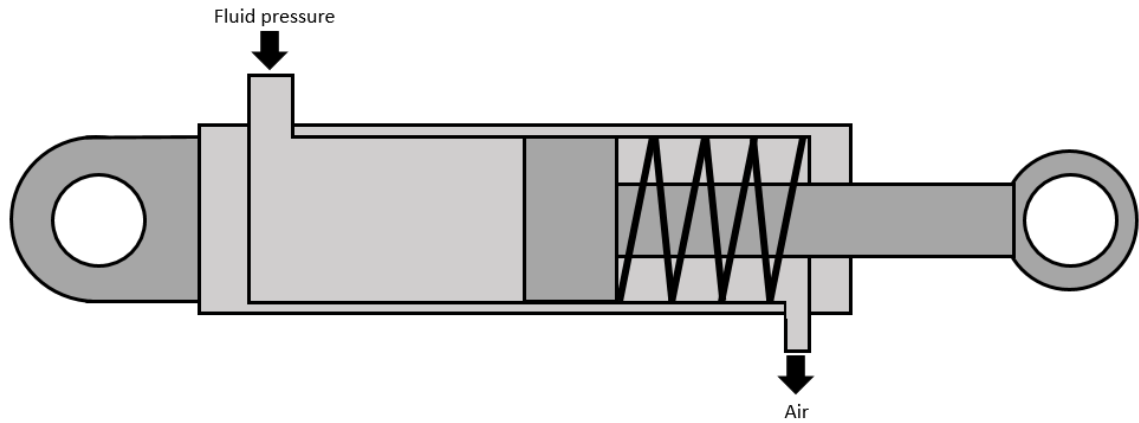


Figure 3. *Simplified structure of a single-acting cylinder.*

Single-acting cylinders are equipped with only one port for fluid to access the cylinder. The cylinder rod moves forward due to the pressure difference in cylinder chambers. The opposing motion is due to external force from, e.g., a spring or mass. Double-acting cylinders are widely used in industrial and mobile applications because they can produce high forces in both motion directions. The simplified structure of the most popular type of double-acting cylinder with a one-sided piston rod is shown in Figure 4.

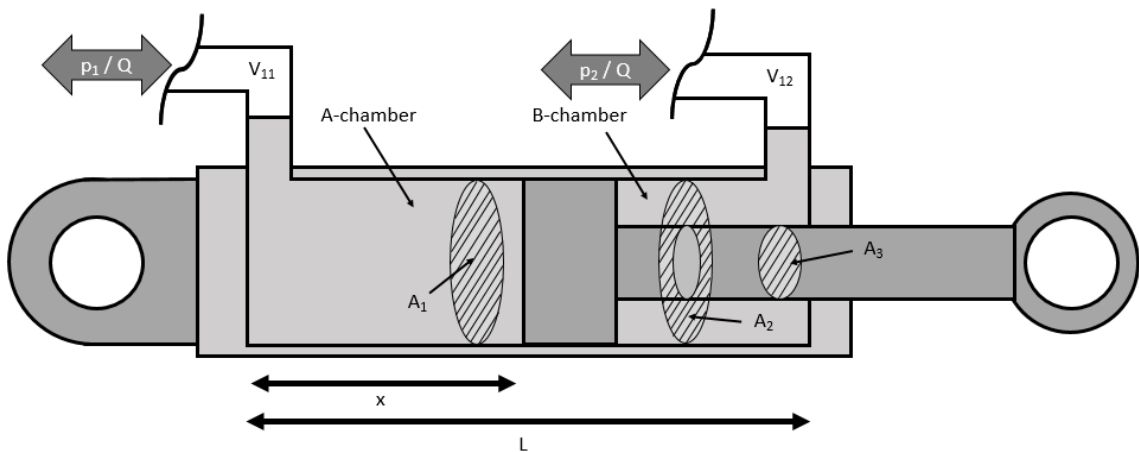


Figure 4. *Simplified structure of a double-acting hydraulic cylinder.*

Motion of a double-acting hydraulic cylinder is due to different pressures in cylinder chambers and different cross-section areas on which these pressures act. The direction of motion can be changed by changing the position of the direction valve spool. In general, the hydraulic cylinder's effective areas are designed in such way that the ratio of the areas A_1/A_2 is two. This way it is possible to obtain the same velocities in both direction by using regenerative circuit. [12] However, this depends on the application, and therefore, the ratio can vary if same velocity in both direction is not a requirement.

2.1.1 Hydraulic cylinder basic equations

The equations to calculate velocity, force and power of the cylinders are well known and presented in different papers. The equations used in this section are derived as in [12]. The velocity of the hydraulic cylinder's piston depends on the flow rate and the effective area of the chamber. Velocity of the piston can be calculated with equation:

$$v = \frac{Q}{A}, \quad (2.1)$$

where Q is flow rate and the A is the area of the piston A_1 or piston rod side area A_2 shown in Figure 3. The flow rate is the same on both sides of the cylinder. The area of the piston rod side can be calculated by subtracting cross-sectional area of the piston rod from the piston side area. Well-known formula for the pressure p can be written as

$$p = \frac{F}{A}. \quad (2.2)$$

The formula for the force produced by hydraulic cylinder is the resultant force between the cylinder chambers and it can be written as

$$F_t = F_1 - F_2 = p_1 \cdot A_1 - p_2 \cdot A_2, \quad (2.3)$$

where p_1 is the pressure on the piston side, p_2 is the pressure on the piston rod side and the areas A_1 and A_2 are the effective areas of the chambers shown in Figure 4. The output power of the hydraulic cylinder can be calculated with equation:

$$P = Q \cdot \left(p_1 - \frac{A_2}{A_1} \cdot p_2 \right) \cdot \eta_t = F \cdot v, \quad (2.4)$$

where η_t is the total efficiency of the hydraulic cylinder. The total efficiency of the cylinder is a combination of mechanical efficiency which is affected by mechanical and hydraulic friction and volumetric efficiency which includes leaks in the cylinder. The total efficiency is not constant, and it depends on e.g., flow rate, pressure, temperature, and fluid properties. [12]

2.1.2 Stiffness of hydraulic cylinder

Hydraulic cylinders can be modelled as two springs in series [13], [14]. According to [14] the stiffness of the springs on both sides of the piston change in different piston positions. The total stiffness of the springs is a combination of the two springs and can be calculated with equation

$$KH_t = KH_A + KH_B, \quad (2.5)$$

where KH_t is the total hydraulic stiffness, KH_A is the stiffness of the piston side and KH_B is the stiffness of the piston rod side [13]. As follows, the piston side stiffness can be written as

$$KH_A = \frac{A_1^2 \cdot B_1}{A_1 \cdot x + V_{11}}, \quad (2.6)$$

where A_1 is the piston area, B_1 is the effective bulk modulus on the piston side, x is the position of the piston and V_{11} is the volume of the hoses or pipes. The stiffness of the piston rod side can be calculated with equation

$$KH_B = \frac{A_2^2 \cdot B_1}{A_1 \cdot (L - x) + V_{12}} \quad (2.7)$$

where A_2 is the piston rod side area, B_2 is the effective bulk modulus on the piston rod side, x is the position of the piston, L is the stroke of the cylinder and V_{12} is the volume of the hoses or pipes on the piston rod side. Substituting Eq. (2.6) and (2.7) into Eq. (2.5) we obtain:

$$KH_t = \frac{A_1^2 \cdot B_1}{A_1 \cdot x + V_{11}} + \frac{A_2^2 \cdot B_1}{A_1 \cdot (L - x) + V_{12}}. \quad (2.8)$$

As shown in Eq. (2.8), the stiffness of the cylinder is highly dependent on the volumes of the chambers. The effective bulk modules for both sides of hydraulic cylinders can be written as

$$\frac{1}{B} = \frac{1}{B_0} + \frac{V_p}{VB_p} + \frac{V_h}{VB_h}, \quad (2.9)$$

where B_0 , B_p and B_h are the bulk modules of oil, pipe and hose, and V_p and V_h are the volumes of the pipe and the hose. Usually, the bulk modules of the pipes and hoses can be neglected if they are short but the volumes of the pipes and hoses should be taken in account. [13] More information about bulk modulus can be found in [14].

2.1.3 Inertia of hydraulic cylinder

The inertia of the oil should be considered when calculating the total inertia of the hydraulic system. According to [15], the effective mass of the incompressible moving fluid can be calculated using the kinetic energy equation:

$$T_f = \frac{1}{2} m_{f,A} \cdot v_{f,A}^2 + \frac{1}{2} m_{f,B} \cdot v_{f,B}^2 = \frac{1}{2} m_{eff} \dot{x}, \quad (2.10)$$

where T_f is the kinetic energy of the fluid, $m_{f,A}$ and $m_{f,B}$ are the masses of the fluid in pipes or hoses and $v_{f,A}$ and $v_{f,B}$ are the velocities of the fluid, m_{eff} is the effective mass

of the fluid and \dot{x} is the velocity of the piston. The velocity of the fluid in pipes or hoses can be calculated using the ratio of the chamber and pipe areas:

$$v_{fluid,A} = \frac{A_A}{A_{pipe,A}} \dot{x}, \quad (2.11)$$

$$v_{fluid,B} = \frac{A_B}{A_{pipe,B}} \dot{x}, \quad (2.12)$$

where $A_{pipe,A}$ and $A_{pipe,B}$ are the areas of the pipes in both sides of the cylinder. The mass of the fluid depends on the fluid's density ρ_f and the area and the volume of the pipes.

$$m_{fluid} = \rho_f \cdot V_{pipe}. \quad (2.13)$$

Substituting Eqs. (2.11) and (2.12) into Eq. (2.10) we obtain:

$$T_f = \frac{1}{2} \left(m_{fluid,A} \left(\frac{A_A}{A_{pipe,A}} \right)^2 + m_{fluid,B} \left(\frac{A_B}{A_{pipe,B}} \right)^2 \right) \dot{x}^2, \quad (2.14)$$

Taking the mass term from Eq. (2.14) and substituting Eq. (2.13), the equation for the effective mass can be written as:

$$m_{eff} = \rho_{fluid} \cdot V_{pipe,A} \left(\frac{A_A}{A_{pipe,A}} \right)^2 + \rho_{fluid} \cdot V_{pipe,B} \left(\frac{A_B}{A_{pipe,B}} \right)^2. \quad (2.15)$$

As can be seen from Eq. (2.15), the inertia of the fluid depends highly on the ratio between chamber areas and pipe areas. [15]

2.1.4 Natural frequency with hydraulic cylinder

Natural frequency is determined at that time when valves or valve on each chamber of the hydraulic cylinder is suddenly closed. At this moment, the hydraulic cylinder and manipulator starts to oscillate. According to [14], the minimum value of the natural frequency is obtained at the position where there are equal amount of fluid in both chambers. As follows, the maximum values can be obtained when the hydraulic cylinder is at minimum or maximum length as the stiffness of the fluid in chamber with lower volume increases. A hydraulic system with high natural frequency has better controllability and an ability to accelerate the load quicker. The natural angular frequency ω_H depends on the stiffness of the actuator, effective mass of the load and on the properties of the fluid as stated earlier. Considering the effective mass of the fluid and using the formula from [14], natural angular frequency of a single hydraulic cylinder can be written as:

$$\omega_H = \sqrt{\frac{KH_t}{(m_{load} + m_{eff})}}, \quad (2.16)$$

where KH_t is the stiffness of the cylinder, m_{load} is the effective load mass and m_{eff} is the effective mass of the fluid. The natural frequency $f_{AR,H}$ can be calculated with equation:

$$f_{AR,H} = \frac{1}{2\pi} \sqrt{\frac{KH_t}{(m_{load} + m_{eff})}}. \quad (2.17)$$

Manipulators with hydraulic cylinders have usually low natural frequency because of the fluid's compressibility. It should be noted that the natural frequencies of a manipulator are not frequencies of the hydraulic cylinders [15].

2.2 Electromechanical linear actuators

Electromechanical linear actuator (EMLA) is a device that converts rotational motion into linear motion or vice versa. The main components of EMLA are a cylinder housing, a thrust tube, attachments, a ball screw or roller screw, a gearbox and motor. A simplified picture of a EMLA with parallel structure is shown in Figure 5.

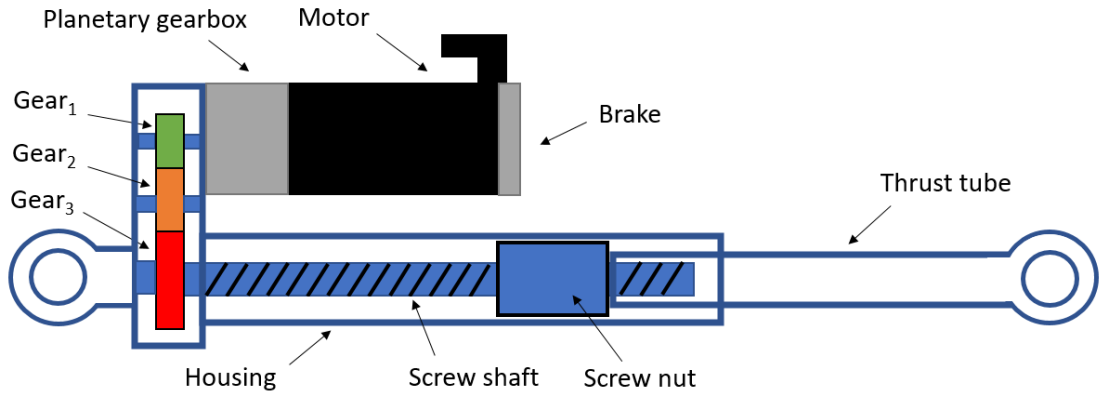


Figure 5. Components of EMLA.

The power transmission chain of the EMLA starts from the motor, which produces torque and rotational speed from the electric power. The gearbox reduces the rotational speed and increases the torque to a useful level. The screw shaft and nut unit change the rotational motion into linear motion. The velocity and the force are proportional to the screw lead.

2.2.1 Screw types

There are three main types of screws and nuts to convert linear motion from rotary motion. The types of the screw are ball screw, lead screw and roller screw. The different types of screws are shown in Figure 6.



Figure 6. *Ball screw, lead screw and roller screw. [16]–[18]*

Ball screw assembly consist of a ball screw and single or double ball nut. The ball screw and ball nut are not in contact as the balls are between them. The rolling elements reduce the friction, and therefore the ball screw efficiency can be over 90 %. The balls recirculate in return channels that are in the ball nut unit which allows the linear motion. [19] In addition, there can be several rows and return channels to raise the static and dynamic force capabilities of the balls screw. Hence, the force distribution between the ball screw and the ball nut are divided between several balls which reduces the local surface pressures. According to [19], the advantages of recirculating ball screws are:

- High efficiency due to rolling contact
- Lack of slide and stick phenomenon between contact surfaces
- Minor wear and flaking in surfaces
- Small torque when starting the movement due to low friction
- Excellent for high-speed use
- Anti-backlash can be made easily by preloading
- Low noise in operation
- High reliability and durability
- High load carrying capacity compared to power screws

The disadvantages of the ball screws are:

- More expensive compared to lead screws
- Velocity should be limited under the critical speed of the ball screw
- Requires good lubrication between contact areas

- Requires service to maintain the efficiency
- Locking the ball screw requires external brake [19].

Lead screws resemble a regular bolt and a nut, but the thread type and tolerances are different. ACME lead screw is standardized and commonly used thread type for lead screws. The surfaces of the lead screw and lead nut are in contact with each other therefore the friction is relatively high compared to ball screws. [19] The advantages of lead screws are:

- High load carrying capacity
- Simple to manufacture and design
- Good positioning tolerance
- Low noise and smooth operation
- Requires little maintenance
- Self-locking. [19]

The disadvantages of lead screws are:

- Efficiency is poor
- High wear and flaking due to sliding contact. [19]

Roller screw (also called planetary roller screws) is more recent invention than the other screw types and was invented at the turn of 1950s. Roller screw is the third type of the screws and it consists of a nut, a screw and rollers. [20] Roller screws are reliable, accurate, and they withstand high forces due to many contact surfaces. On the other hand, the friction is higher compared to ball screws and they are more expensive to manufacture. [21] According to [21], the advantages of roller screws are:

- Highest positioning tolerance
- Longest life
- Highest load capacity
- Smaller leads available. [21]

The disadvantages of the roller screws are:

- Higher friction and heat generation
- Efficiency is lower compared to ball screws

- High manufacture costs due to complex structure. [21], [22]

Selection of the screw type depends on the application and required performance. Ball screws and roller screws are most used screw types because their capabilities are better compared to lead screws. Ball screws are widely used in machine tools and other applications but if extreme reliability and lifetime is needed roller screws outperform ball screws. For this reason, roller screws are used in machines such as the Mars Rover [23] that operate in demanding environments.

2.2.2 Sizing of EMLA

The procedure of sizing a EMLA is an iterative process. The process is the same for all types of screws and manufactures use similar procedures to select screws for EMLAs. The first step is to calculate the fatigue life of the screw. Fatigue life calculations for ball screws are standardized and they are based on the methods used to calculate the fatigue life of angular contact ball bearing. However, there is disagreement in the literature about this calculation method because the calculations ignore e.g. stroke of the screw assembly, lead of the screw and number of ball circuits [24]. In this section, the fatigue life calculations are based on methods described in standard ISO 3408-5:2006 [25] which are widely used among different manufacturers. These calculations are for a screw that is not preloaded but the calculations for a preloaded screw can be found in [25]. Another standard that manufacturers use is JIS B1192-1997 which has minor differences compared to DIN ISO 3408 [26]. Iterative procedure for selecting the screw is shown in Figure 7.

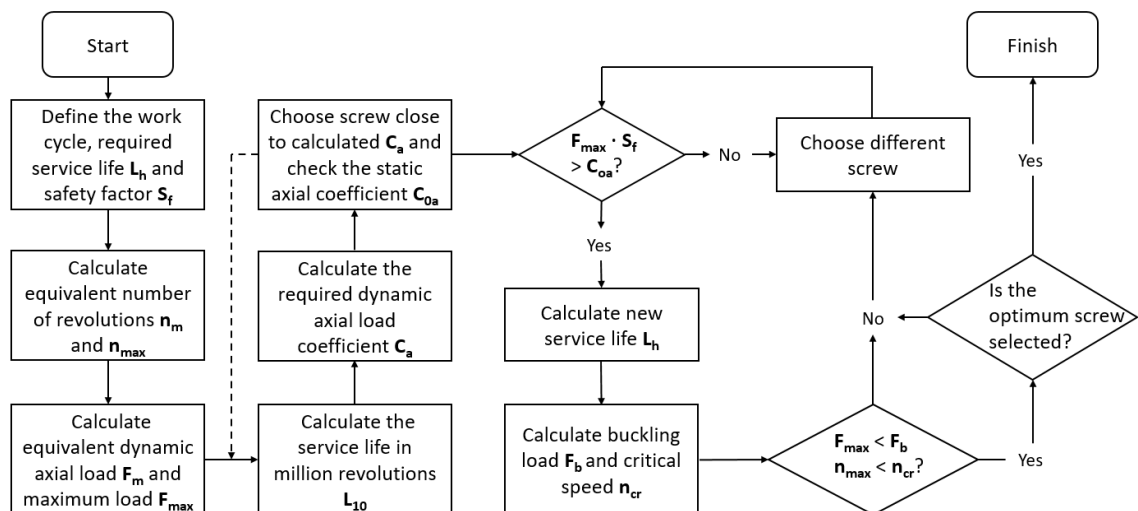


Figure 7. Process for sizing a screw system.

First step in sizing the ball screw is to define the work cycle which includes measuring the forces and velocities from the application. If the purpose is to replace a hydraulic

cylinder with EMLA, the forces can be measured from the pressures in the cylinder chambers, and the velocities with e.g., linear sensors or from joints with angle sensors. In addition, the required service life L_h and the safety factor S_f should be selected. Next, the equivalent number of revolutions and the maximum rotational speed are calculated. The rotational speed can be calculated with equation:

$$n_i = \frac{v_i}{P_h} \cdot 60, \quad (2.18)$$

where n_i is the rotational speed in revolutions per minute, v_i is the linear velocity and P_h is the lead of the screw. The equivalent number of revolutions n_m can be written as:

$$n_m = \sum_{i=1}^n \frac{q_i}{100} \cdot n_i, \quad (2.19)$$

where q_i is the share of a single time step in the total time and n_i is the rotational speed in that time step. The equivalent number of revolutions can also be replaced by the equivalent velocity v_m , but the equivalent number of revolutions is required to calculate the service life in hours. Next step is to calculate the equivalent axial load F_m , and it can be written as:

$$F_m = \sqrt[3]{\sum_{i=1}^n \left(F_i^3 \cdot \frac{q_i}{100} \cdot \frac{n_i}{n_m} \right)}, \quad (2.20)$$

where F_i is the force in different time steps. Then, the required service life in revolutions L_{10} can be calculated with equation:

$$L_{10} = L_h \cdot n_m \cdot f_n \cdot 60, \quad (2.21)$$

where L_h is the required service life in hours and f_n is the share of the screw operation in machine operation. With a 90 % probability, the screw will last this service life. Once the equivalent axial load and required service life in revolutions is calculated, dynamic axial load C_a can be calculated from equation

$$C_a = F_m \cdot \sqrt[3]{\frac{L_{10}}{10^6}}. \quad (2.22)$$

Next, based on the dynamic axial load, the maximum force, the safety factor and the screw lead, a screw can be selected from the manufactures' tables. If the screw with the selected lead and calculated dynamic axial load cannot be found in the manufacturer's catalog, the required service life in revolutions and dynamic axial load must be recalculated with a new screw lead. Then the new screw can be selected based on these calculations. After this, the required static axial load C_{0a} can be written as

$$C_{0a} = F_{max} \cdot S_f, \quad (2.23)$$

where F_{max} is the maximum axial force and S_f is the safety factor. If the static axial load is acceptable, new service life can be calculated with Eqs. (2.21) and (2.22). Solving Eq. (2.22) for L_{10} and calculating the new service life with screw's dynamic axial load and substituting the result into Eq. (2.21), new service life in hours can be determined. If the service life is acceptable, the buckling load F_b and critical speed n_{cr} shall be evaluated next. The buckling load depends on the material's modulus of elasticity E , screw's area moment of inertia I and effective length of the screw l_e . Euler's well-known formula for calculating the buckling load is (see e.g. [27], [28]):

$$F_b = \frac{\pi^2 \cdot E \cdot I}{l_e^2}. \quad (2.24)$$

The effective length depends on the screw's support method. The supports and the buckling loads are shown in Figure 8.

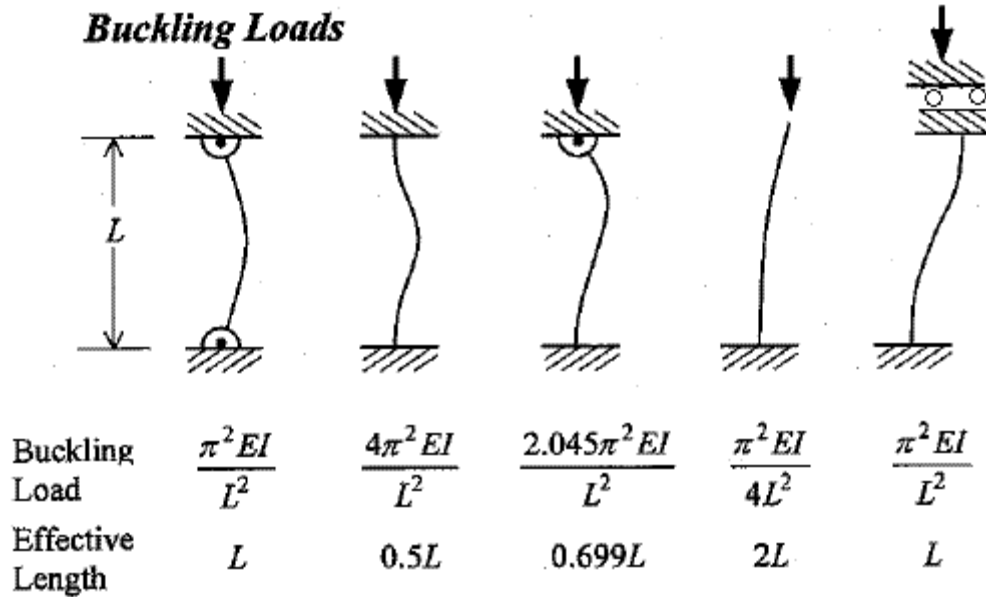


Figure 8. Buckling loads and effective lengths. [29]

The support method depends on the application. If the EMLA is supported with rod eyes, the support method is the first shown in Figure 8. Last, the critical speed n_{cr} is the lowest rotational speed at which the shaft begins to resonate. This phenomenon is due to the fact that the center of gravity (CoG) is not on the axis of rotation [30]. According to [30], [31], critical speed can be calculated by:

$$n_{cr} = \frac{60 \cdot \lambda^2}{2\pi \cdot L^2} \sqrt{\frac{E \cdot I \cdot g}{\gamma \cdot A}}, \quad (2.25)$$

where L is the unsupported length of the shaft, γ is the specific weight of screw shaft, A is the cross-sectional area of the shaft and λ the factor that depend on the support condition. Values for lambda are shown in Table 1.

Table 1. Support condition and value for factor λ . [31]

Support condition	λ
<i>Fixed – Simple support</i>	3.927
<i>Fixed – Fixed support</i>	4.730
<i>Fixed support – Free</i>	1.875
<i>Simple – Simple support</i>	π

After the process of selecting the screw is finished, the stiffness and inertia of the EMLA can be calculated.

2.2.3 Stiffness of EMLA

Stiffness of the EMLA depends on individual stiffnesses of the components and it is important when considering the accuracy and controllability of the EMLA. The components affecting total stiffness can be divided into different sections:

- Ball screw stiffness
- Gearbox stiffness
- Planetary gearbox stiffness
- Bearing stiffness
- Coupling stiffness.

The stiffness components are shown in Figure 9.

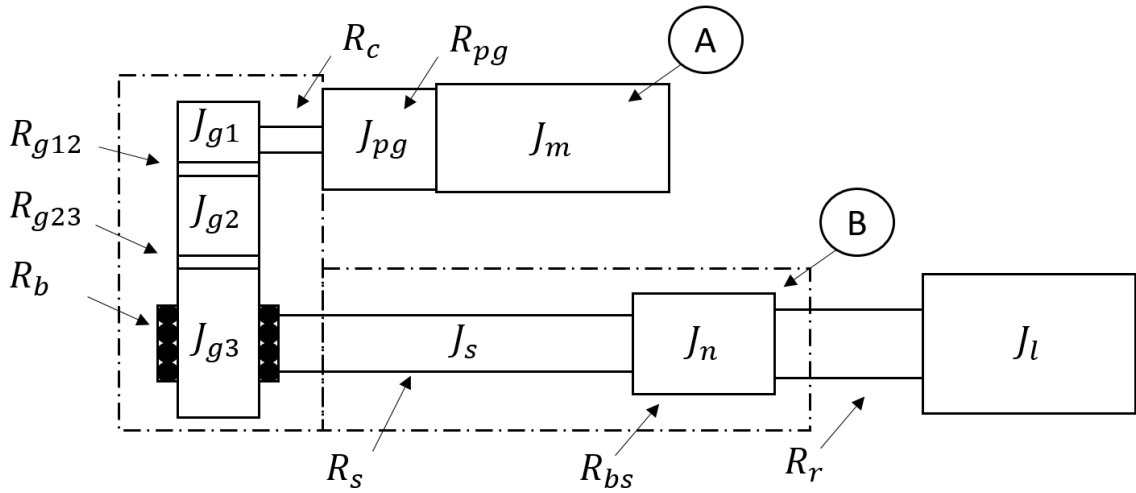


Figure 9. Stiffness components of EMLA.

Total stiffness of the system can be calculated at different points in the system. For example, the rotational stiffness at point A can be calculated by reflecting the stiffnesses of the components to the motor shaft and as translational stiffness by reflecting the same stiffnesses to point B in the nut unit. Gear ratio of a planetary gearbox and gearbox with spur gears affects the stiffness of the system. In addition, the ball screw acts as a gearbox therefore the ball screw lead affects the total stiffness. The stiffness at point A can be calculated with equation:

$$R_{A,tot} = \left[\left[\left(\left(\frac{1}{R_L} \right) \cdot \left(\frac{2\pi}{P_h} \right)^2 + \frac{1}{R_{g23}} \right) \cdot i_{13}^2 + \frac{1}{R_{g12}} \cdot i_{12}^2 + \frac{1}{R_c} \right] \cdot i_{pg}^2 + \frac{1}{R_{pg}} \right]^{-1}, \quad (2.26)$$

where

$$\frac{1}{R_L} = \frac{1}{R_{bs}} + \frac{1}{R_b} + \frac{1}{R_r}.$$

The parameters in Eq. (2.26) are: R_A is rotational stiffness at point A, R_{bs} is ball screw system's stiffness, R_b is bearing stiffness, R_r is stiffness of the rod, P_h is ball screw's lead, i_{ij} is gear ratio between two mating gears, i_{pg} is gear ratio of planetary gearbox, R_{gij} is rotational stiffness between two mating gears, R_c is coupling's stiffness and R_{pg} is planetary gearbox's stiffness which is usually given to input shaft in manufacturers' tables. In most cases, stiffness of the gearbox and planetary gearbox can be neglected. The stiffness at point B can be written similarly:

$$R_{B,tot} = \left[\left[\left(\frac{1}{R_{pg}} \cdot \left(\frac{1}{i_{pg}} \right)^2 + \frac{1}{R_c} \right) \cdot \left(\frac{1}{i_{13}} \right)^2 + \frac{1}{R_{g12}} \cdot \left(\frac{1}{i_{23}} \right)^2 + \frac{1}{R_{g23}} \right] \cdot \left(\frac{P_h}{2\pi} \right)^2 + \frac{1}{R_L} \right]^{-1}. \quad (2.27)$$

Relation between stiffness in point A and point B can be calculate with equation:

$$R_{B,tot} = R_{A,tot} \cdot \left(\frac{2\pi \cdot i_{tot}}{P_h} \right)^2, \quad (2.28)$$

where i_{tot} is the total gear reduction in the system. In addition, the relation the other way around is:

$$R_{A,tot} = R_{B,tot} \cdot \left(\frac{P_h}{2\pi \cdot i_{tot}} \right)^2. \quad (2.29)$$

The stiffness of the ball screw system R_{bs} is always smaller than the smallest individual stiffness. The stiffness of screw shaft R_s , screw nut unit and R_{nu} can be found from the manufacturer's tables or they can be calculated. It should be noted that the values given in manufacturer's tables are valid only for single load application. According to [32], the stiffness of the ball screw system is:

$$\frac{1}{R_{bs}} = \frac{1}{R_s} + \frac{1}{R_{nu}}. \quad (2.30)$$

Design parameters for calculating the stiffness of the screw shaft and screw nut are shown in Figure 10.

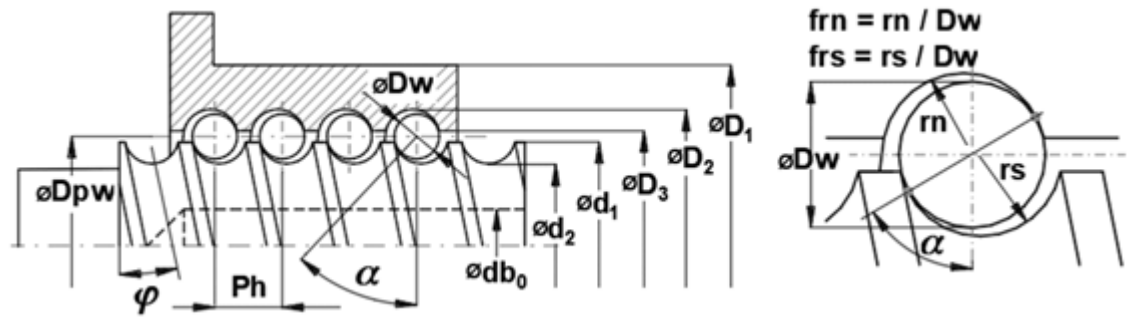


Figure 10. Ball screw design parameters. [33]

The nomenclature for dimensions of the ball screws depends on the source. The nomenclature used in these calculation are from [33] and [32]. The ball screw dimensions are explained in Table 2.

Table 2. Nomenclature for ball screw. [33]

Parameter	Explanation
l_s	Position of the nut
L	Distance between supports
i_z	Number of loaded turns

P_h	Lead of ball screw
φ	Lead angle
E	Modulus of elasticity
α	Nominal contact angle
D_1	Ball nut body diameter
D_2	Ball nut root diameter
D_3	Ball nut internal diameter
d_1	Nominal diameter of screw
d_2	Ball screw shaft root diameter
db_0	Screw shaft's hole diameter
D_c	Diameter of contact point between nut and balls
d_c	Diameter of contact point between balls and shaft
D_{pw}	Pitch circle diameter
D_w	Ball diameter
r_n	Nut unit's ball track radius
r_s	Screw shaft's ball track radius

The stiffness of the nut unit can be calculated from equation:

$$R_{nu} = \frac{R_{n/s} \cdot R_{b/t}}{R_{n/s} + R_{b/t}}, \quad (2.31)$$

where $R_{n/s}$ is the stiffness between nut body and screw shaft and $R_{b/t}$ is the stiffness in the ball track area. According to [33], [34], the stiffness between the ball nut body and screw shaft can be calculated with equation:

$$R_{n/s} = \frac{2\pi \cdot I_z \cdot P_h \cdot E \cdot \tan^2 \alpha}{\left(\frac{D_1^2 + D_c^2}{D_1^2 - D_c^2} \right) 10^3}. \quad (2.32)$$

The contact diameter D_c between the balls and nut can be written as:

$$D_c = D_{pw} + D_w \cos \alpha. \quad (2.33)$$

The lower contact diameter between the balls and the screw shaft affects the stiffness of the screw shaft and it can be calculated with equation:

$$d_c = D_{pw} - D_w \cos \alpha. \quad (2.34)$$

In addition, the way the screw shaft is supported affects the stiffness of the shaft. If the screw shaft is mounted only from one end, the axial stiffness of the screw shaft can be calculated by:

$$R_{s,ax} = \frac{\pi \cdot (d_c^2 - db_0^2) \cdot E}{4l_s \cdot 10^3}. \quad (2.35)$$

If both ends of the screw shaft are fixed, the stiffness can be written as:

$$R_{s,ax} = \frac{\pi \cdot (d_c^2 - db_0^2) \cdot E}{4l_s \cdot 10^3} \cdot \frac{L}{(L - l_s)}. \quad (2.36)$$

The minimum stiffness for the shaft is when $l_s = L/2$. [33] Rotational stiffness of the screw shaft can be calculated with equation:

$$R_{s,rot} = \frac{G_s \cdot \pi \cdot d_c^4}{32l_s}, \quad (2.37)$$

where G_s is the screw shear modulus [35]. It should be noted that rotational stiffness has very small impact on the total ball screw stiffness [36]. The Eq. (2.32) is same for coupling stiffness R_c . Total stiffness of the screw shaft is:

$$R_s = \left(\frac{1}{R_{s,ax}} + \left(\frac{P_h}{2\pi} \right)^2 \cdot \frac{1}{R_{s,rot}} \right)^{-1}. \quad (2.38)$$

According to ISO 3408-4:2006 [32] standard, the axial deflection due to Hertz stress can be calculated with equation:

$$\Delta l_{b/t} = \left(\frac{F}{k \cdot I_z} \right)^{2/3}, \quad (2.39)$$

where F is force and stiffness characteristic k can be written as:

$$k = \frac{z_1 \sin^{5/2} \alpha \cdot \cos^{5/2} \lambda}{C_E^3 \cdot C_K^{3/2}}, \quad (2.40)$$

where z_1 is number of balls that are loaded effectively, λ is lead angle of the screw, C_E is the material constant and C_k is the geometry constant. Effectively loaded balls z_1 can be calculated by:

$$z_1 = \left(\frac{D_{pw} \cdot \pi}{\cos \varphi \cdot D_w} - z_2 \right)_{\text{integer}}, \quad (2.41)$$

where z_2 is the number of the unloaded balls in the recirculation system and it is used only in ball screws where balls go into the return channel after one rotation of the screw shaft. [32]

According to [32], parameter C_E depends on the material properties of the screw shaft, balls and nut unit and it can be calculated with equation:

$$C_E = \sqrt[3]{11550 \frac{E_{0s,n} + E_{0b}}{E_{0s,n} \cdot E_{0b}}}, \quad (2.42)$$

where E_{0b} is the elastic modulus of balls and $E_{0s,n}$ can be written as:

$$E_{0s,n,b} = \frac{E_{s,n,b}}{1 - \frac{1}{m_{s,n,b}^2}}, \quad (2.43)$$

where $E_{s,n,b}$ is the elastic modulus of the screw shaft, the nut unit and the balls, and $m_{s,n,b}$ is the Poisson's ratio of these components.

Next, the constant C_K can be calculated with equations that depend on the geometric properties of the ball screw. First, reciprocal radius of curvature $\sum \rho_s$ between the screw shaft and balltrack/ball can be obtained from equation:

$$\sum \rho_s = \frac{4}{D_w} - \frac{1}{f_{rs} \cdot D_w} + \frac{2 \cdot \cos \alpha}{D_{pw} - D_w \cdot \cos \alpha}. \quad (2.44)$$

Reciprocal radius of curvature between the nut and balltrack/ball can be calculated with equation:

$$\sum \rho_n = \frac{4}{D_w} - \frac{1}{f_{rn} \cdot D_w} - \frac{2 \cdot \cos \alpha}{D_{pw} + D_w \cdot \cos \alpha}. \quad (2.45)$$

Parameters f_{rs} and f_{rn} in Eqs. (2.37) and (2.38) are conformity ratios between the ball, the screw shaft and the ball nut, respectively. Next, cosine of the ratios between semi-major and semi-minor axes of the contact ellipses $\cos(\tau_{s,n})$ can be calculated with equations:

$$\cos \tau_s = \left| \frac{-\frac{1}{f_{rs} \cdot D_w} + \frac{2 \cdot \cos \alpha}{D_{pw} - D_w \cdot \cos \alpha}}{\sum \rho_s} \right|. \quad (2.46)$$

$$\cos \tau_n = \left| \frac{-\frac{1}{f_{rn} \cdot D_w} + \frac{2 \cdot \cos \alpha}{D_{pw} + D_w \cdot \cos \alpha}}{\sum \rho_n} \right|. \quad (2.47)$$

Auxiliary values $Y_{s,n}$ can be obtained from equation:

$$Y_{s,n} = 1,282[-0,154(\sin \tau)^{1/4} + 1,348(\sin \tau)^{1/2} - 0,194 \sin \tau], \quad (2.48)$$

where $\sin \tau = \sqrt{1 - \cos \tau^2}$. Last, the parameter C_K can be calculated with equation:

$$C_K = Y_s \sqrt[3]{\sum \rho_s} + Y_n \sqrt[3]{\sum \rho_n}. \quad (2.49)$$

By deriving the Eq. (2.39) with respect to force F , the stiffness for the ball/ball track area can be formed:

$$R_{b/t} = \frac{\Delta F}{\Delta l_{b/t}} = \frac{3}{2} \sqrt[3]{F(I_z \cdot k)^2}. \quad (2.50)$$

It should be noted that $R_{b/t}$ is not linear and it depends on the applied load. According to [34], the machining inaccuracies affects the stiffness of the ball nut unit therefore correction factor f_{ar} shall be used to account these errors. The correction factor depends on the standard tolerance grade of the ball screw. The tolerance factors are shown in Table 3.

Table 3. Standard tolerance grades and correction factors.[32]–[34]

Standard tolerance grade	0, 1	3	5	7, 10
Factor f_{ar}	0.6	0.55	0.5	0.4

Now, the rigidity of the ball nut unit with correction factor can be written as:

$$R_{nu,ar} = f_{ar} \cdot R_{nu}. \quad (2.51)$$

Last, the total rigidity of the ball screw assembly can be calculated with equation:

$$R_{bs} = \left(\frac{1}{R_s} + \frac{1}{R_{nu,ar}} + \frac{1}{R_{b/t}} \right)^{-1}. \quad (2.52)$$

According to [32], the stiffness of the ball screw system can be increased by preloading the ball screw because this affects the axial stiffness of preloaded nut body and screw shaft $R_{n/s,pr}$ as the stiffness is

$$R_{nu,pr} = 2 \cdot R_{nu}. \quad (2.53)$$

In addition, preload increases the stiffness of the ball/ball track area $R_{b/t,pr}$ and eliminates the backlash when $0 < F_e \leq F_{lim}$, where F_e is external force and F_{lim} is obtained from equation:

$$F_{lim} = 2^{3/2} \cdot F_{pr}. \quad (2.54)$$

Preload force F_{pr} varies between manufacturers and typical values are under 10 % [37]. In fatigue life calculations for preloaded ball screw, the preload is set to 60 % of the original preload because the wear between the components affects the preload [32], [38].

2.2.4 Inertia of EMLA

The inertia of the EMLA depends on the inertia of individual components of the system. The inertial components of the system are shown in Figure 11.

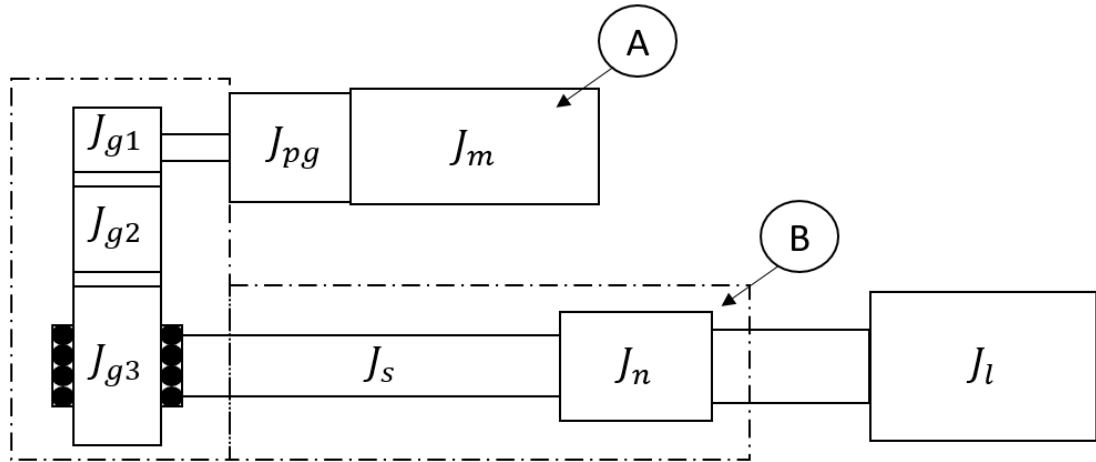


Figure 11. Inertial components of EMLA.

The inertia of the system can be calculated as rotational inertia at point A and as translational inertia at point B in the same way as the stiffness of the system. The inertia components of the system are:

- Motor inertia J_m
- Planetary gearbox inertia J_{pg}
- Gear inertia J_{gi}
- Ball screw shaft inertia J_s

- Ball screw nut unit mass J_n
- Load inertia J_l .

The inertia of the components is usually given in manufacturers' tables, but approximate results can be calculated for the gears and ball screws. Inertia of the gears can be approximated with equation:

$$J_g = \frac{1}{8} \cdot m_g \cdot (D_g)^2, \quad (2.55)$$

where D_g is the diameter of the gear. The mass of the gear can be written as:

$$m_g = \frac{\pi \cdot D_g^2}{4} \cdot t_g \cdot \rho_g, \quad (2.56)$$

where t_g is the gear's thickness and ρ_g is density of the gear. If the EMLA is used to actuate a joint and the load is assumed to be a point mass, inertia of the load J_l acting the cylinder can be calculated with equation:

$$J_l = m_l \cdot \frac{L_l^2}{r^2}, \quad (2.57)$$

where m_l is mass of the load, L_l is the distance to link's CoM and r is the moment arm.

The total inertia of the EMLA at point A can be calculated with equation:

$$J_{A,tot} = \left[\left((J_l + J_n) \cdot \left(\frac{P_h}{2\pi} \right)^2 + J_{g3} + J_s \right) \cdot \left(\frac{1}{i_{13}} \right)^2 + J_{g2} \cdot \left(\frac{1}{i_{12}} \right)^2 + J_{g1} \right] \cdot \left(\frac{1}{i_{pg}} \right)^2 + J_{pg} + J_m, \quad (2.58)$$

and at point B with equation:

$$J_{B,tot} = \left[((J_m + J_{pg}) \cdot i_{pg}^2 + J_{g1}) \cdot i_{13}^2 + J_{g2} \cdot i_{23}^2 + J_{g3} + J_s \right] \cdot \left(\frac{2\pi}{P_h} \right)^2 + J_n + J_l. \quad (2.59)$$

If the component is not in rotational motion, the inertia of the component is the mass of the component. There is same relation between inertia as in stiffness at point A and B. The relation between point A and B are [39], [40]:

$$J_B = J_A \cdot \left(\frac{2\pi \cdot i_{tot}}{P_h} \right)^2, \quad (2.60)$$

$$J_A = J_B \cdot \left(\frac{P_h}{2\pi \cdot i_{tot}} \right)^2. \quad (2.61)$$

In general, the inertias of some components can be disregarded in the calculations since gear ratio reduces the inertia by a factor of gear ratio squared. For this reason, the inertia of the motor and the load are predominant.

2.2.5 Natural frequencies of EMLA

Natural frequencies can be calculated at each point in the system. The frequencies of the oscillations are the same at these points. Well-known method for modelling electro-mechanical system dynamics is to use 2-DOF mechanical model shown in Figure 12.

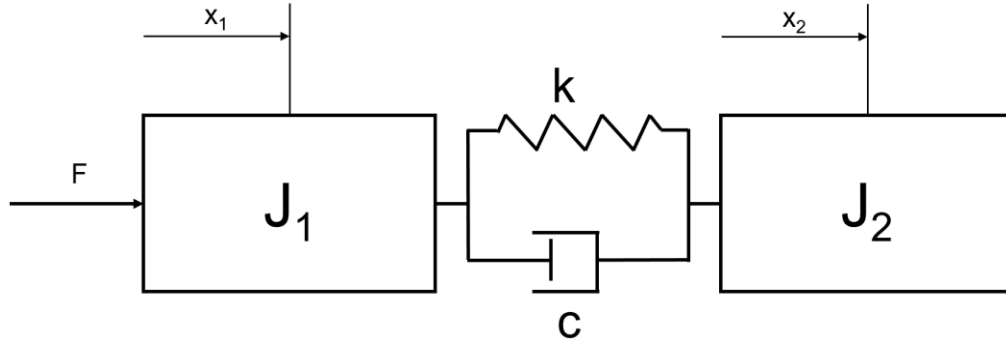


Figure 12. 2-DOF mechanical model. [41]

A system can be modeled with greater number of degrees of freedom if the intention is to identify the components with lowest natural frequencies. If the object is to model dynamic behavior of the system, 2-DOF model is sufficient. [41]

According to [42], there are two frequencies, antiresonance frequency F_{AR} and resonance frequency F_R , in the system. If viscous damping is neglected, the antiresonance frequency, can be calculated with equation:

$$F_{AR,E} = \frac{1}{2\pi} \sqrt{\frac{R_{tot}}{J_l}}, \quad (2.16)$$

where R_{tot} is the total stiffness of the system and J_{load} is the load acting on the actuator. This frequency is the natural frequency of the load oscillation. The second frequency is called resonance frequency F_R :

$$F_{R,E} = \frac{1}{2\pi} \sqrt{\frac{R_{tot} \cdot (J_m + J_{tot})}{J_m \cdot J_{tot}}}, \quad (2.16)$$

where J_m is the inertia of the motor and J_{tot} is the total inertia which includes the inertias of individual components between the motor and the load. At this frequency, both motor and load are oscillating. In this thesis, the natural frequencies are compared when there is zero flow in hydraulic cylinder and EMLA is locked with brake. This means that the natural frequencies obtained by calculation and simulation are antiresonance frequencies.

3. ROBOTS

The word “Robot” was used the first time in beginning of the 1920’s by Karel Čapek in his spectacle, in which mechanical men were forced to work on a production line [43]. According to Zamalloa et al [43], the generation of robotics can be divided into four different groups:

- Generation 0
 - Pre-robots (< 1950)
- Generation 1
 - First Manipulators (1950 – 1967)
- Generation 2
 - Sensorized robots (1968 – 1977)
- Generation 3
 - Industrial robots (1978 – 1999)
- Generation 4
 - Intelligent robots (> 2000).

Use of manipulators in industrial application began 1950’s but before that, pneumatic and hydraulic machines were used in manufacturing processes. These machines were unable to perform any calculations and required humans to control them. [43] However, the first mobile robot called ELSIE (Electro-Light-Sensitive Internal-External) was invented in the late 1940s [44], [45]. ELSIE was able to navigate towards light with the help of photo-electric cell [44]. The next generation introduced simple control algorithms and numerical controlled (NC) machines and due to this, the first industrial robot UNIMATE was made for industrial purposes. These robotic manipulators were able to do simple tasks e.g., pick and place tasks. Robots with sensors was the next step in development of industrial robots. These robots were equipped with various sensors that could be used to observe the environment. In addition, one of the most famous mobile robot SHAKEY by Stanford Research Institute (SRI) was developed in the late 1960s and the first six-axis industrial robot FAMULUS by KUKA in the early 1970s. [43] SHAKEY had capabilities such as navigation and object rearrangement [46]. Other milestone of mobile robotics in the 1970s was first mobile robot Lunokhod-1 on the moon [46]. Mobile robots SHAKEY and Lunokhod-1 are shown in Figure 13.

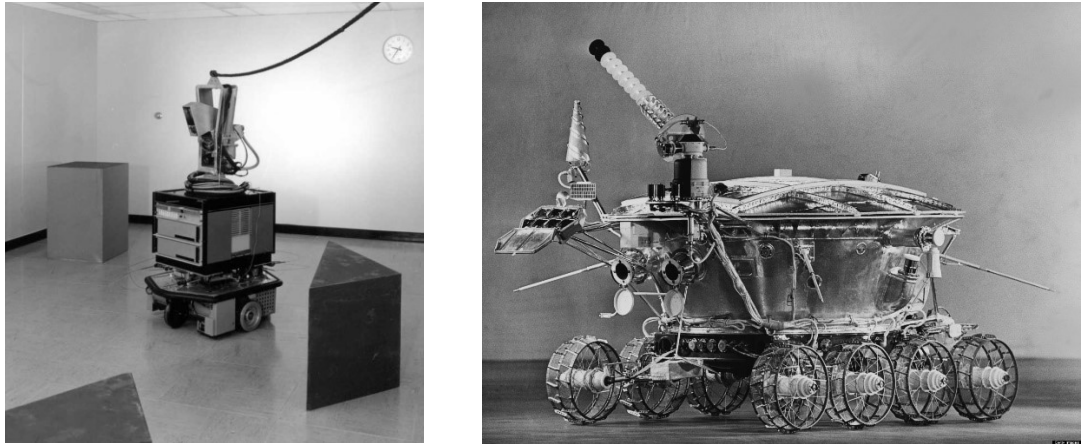


Figure 13. Pictures of SHAKEY and Lunokhod-1. [47], [48]

Generation 3 started an era where investments in robots increased significantly. In this era, new programming languages and re-programmable robots were developed. [43] One of the most significant development in the 1980s was a direct drive arm which eliminated the need of chain systems and intermediate gears [49]. Between 1980 and 2000 there were innovations in kinematic structures [49] but no major innovation in the field of robotics [43]. At the end of the generation 3, Sojourner, the first mobile robot in Mars landed in 1997 [50]. Generation 4, which is ongoing, includes advanced computers and technologies which can adapt to new environments. New technology has made robots available to everyone. The next generation of robots will bring robots and humans closer together to collaborate with each other. [43]

In this chapter, the limitations of industrial robots and mobile robots are discussed. In section 3.1, various industrial robots and their technologies are reviewed, and problems are discussed. Section 2.2 reviews the state-of-the-art mobile manipulators and discusses the problems with industrial robots in mobile applications.

3.1 High payload industrial robots

Industrial robots are used for tasks that are unsuitable for humans. These tasks are usually repetitive, tedious, and dangerous in nature. Industrial robots are beneficial in processes where high quality and productivity are essential. [51] Nowadays, industrial robots are characterized with high-speed, high payload and accuracy capabilities but their features increase their mass.

There are different industrial robot manufacturers such as ABB, Fanuc and KUKA. These manufacturers offer robots with high payload capabilities. Figure 14 shows robots with the highest payloads from these manufacturers.



Figure 14. ABB IRB8700, Fanuc M-2000ia/2300 and KUKA KR1000 titan. [52]–[54]

Robots from ABB, Fanuc and KUKA are used for handling heavy workpieces fast and precisely. All these robots have six axes with 6-DOF wrists, and they use different methods to achieve high payloads. ABB uses only one motor and gearbox at each axis compared to Fanuc and KUKA that use two motors for at least the second and third axes [52]–[54]. All the robots have counterbalance for second axis but only ABB and Fanuc have passive counterbalance mechanism for the third axis. Regarding the counterbalance cylinders, Fanuc and Kuka have both one counterbalancing cylinder behind the structure, but ABB has two identical cylinders side by side. In addition, ABB's and KUKA's third joint is actuated with parallelogram linkage from the same axis as the second joint, and therefore the motor and gearbox weight do not introduce torque to the second axis. These balancing methods reduce the required torque at each axis.

3.2 Limitations of industrial robots in mobile applications

Industrial robots have certain downsides that limit their use in mobile applications. Most significant limitation is their weight compared to their payload and reach [55]. According to survey [55], small size industrial robots have 5 % payload of their weight and larger size robots payload to weight ratio is about 1:5. Industrial robots discussed at previous section have high payloads which introduce weight in their structure. Weight, payload and reach from datasheets are shown in Table 4.

Table 4. Industrial robot specification. [52]–[54]

Robot	ABB IRB8700	Fanuc M-2000ia/2300	KUKA KR1000 titan
Weight	4575 kg	11000 kg	4690 kg
Payload	1000 kg	2300 kg	1300 kg

Reach	3500 mm	3734 mm	3202 mm
Payload to weight ratio	21,1 %	20,9 %	27,7 %

When comparing the payloads between these robots, Fanuc has the highest payload of 2300 kg, KUKA up to 1300 kg and ABB up to 1000 kg. The maximum payload of ABB is given for wrist down position and for KUKA in palletizing mode. KUKA's KR1000 titan has the highest payload to weight ratio but the reach is the lowest. On the other hand, ABB and KUKA have three to four times higher maximum speeds of the joints. [52]–[54] As the robot weights are high, considerable amount of energy is used for moving the structure rather than the load. The reason for the high weight is the accuracy requirements as the components of the robots must be rigid. [55]

3.3 Mobile manipulators

Mobile manipulators can be defined as robots with a mobile platform and one or more manipulators. These manipulators are fixed on the top surface of the mobile platform. Compared to industrial robots, mobile manipulators have larger workspace since they are not fixed to the ground. Mobile manipulators are used in various environments such as construction sites, nuclear power plants, manufacturing facilities or hazardous areas. [56]

Different manipulators and mobile platforms are used depending on the application where mobile manipulators are used. KUKA has developed a mobile manipulator which consist of the KUKA omniMove platform and an interchangeable industrial robot from KR Quantec series. The mobile manipulator is designed to work in manufacturing environments with high precision navigation. KUKA KRM QUANTEC has very large mobile platform as shown in Figure 15. [57]



Figure 15. KUKA KMR QUANTEC. [57]

KUKA omniMove platform can weight up to 15000 kg and its payload capacity is limited to 45000 kg including the robot. There are several options for the robot to mount on the platform, but the largest robot, KR 300 R2500 ultra, has maximum payload of 350 kg. This means that the robot cannot lift loads which the platform can carry. [58]

Different vehicles with robots have been made for harsh environments for various applications including search and rescue, sampling soil or hazardous objects and to gather information from areas where humans cannot enter. Two mobile manipulators for hazardous missions are shown in Figure 16.

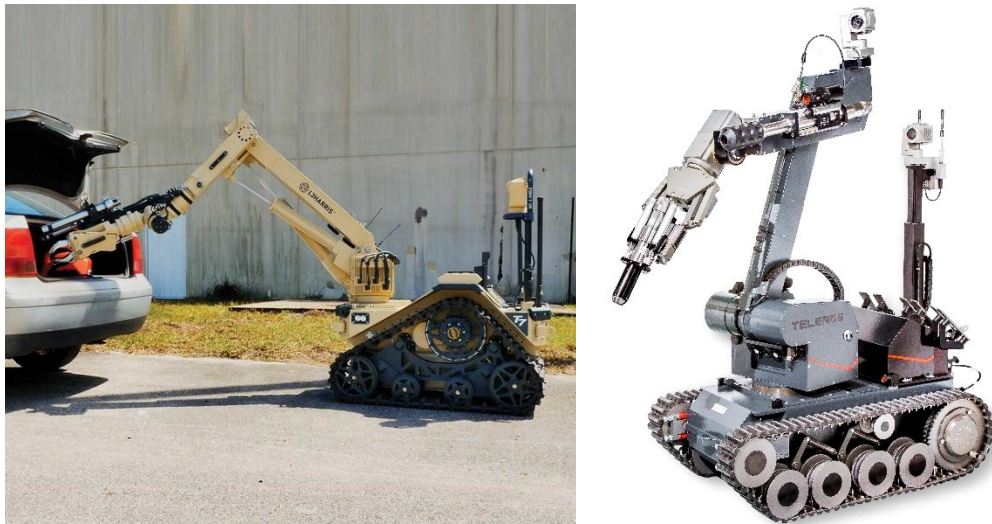


Figure 16. L3Harris T7 and Telerob tEODor EVO. [59], [60]

L3Harris T7 is a robotic system which is used for handling hazardous materials, military and police missions, and for situations which are too dangerous for humans. T7 uses EMLAs to actuate two force-intensive joints which is different compared to widely used configuration where all the joints are driven with motors and gearboxes. On the other hand, the wrist of the robot and base rotation are driven with motors and gearboxes. T7

has lift capacity of 113 kg near the chassis and 27 kg when the manipulator is fully extended. The specifications are decent for a mobile manipulator which weighs 322 kg. [59] The second mobile manipulator, Telerob tEODor EVO, in Figure 16 is used for same kind of applications as T7. The structure of tEODor EVO is different compared to T7 as all the joints are driven with motors and gearboxes. This configuration expands the mobility of the joints but may reduce the lifting capacity of the mobile manipulator. TEODor EVO has circa 10 % lower payload capacity compared to T7 and it weighs about 19 % more. [60]

Rough terrain mobile manipulators with high payloads are rare. Figure 17 presents a high payload mobile manipulator which is called large unmanned ground vehicle (LUGV) developed by Metalliance. [61]



Figure 17. LUGV. [61]

LUGV is different from the mobile manipulators presented earlier. It weighs 4000 kg and the joints are hydraulically actuated with hydraulic cylinders and motors. The power source for LUGV is diesel engine that drives hydraulic pumps. This allows different equipment, such as jackhammer or gripper, to be attached to the end-effector. [61]

There are many differences between the mobile manipulators which allows them to work in different environments. KUKA KMR QUANTEC is the most accurate and it has the highest payload manipulator and platform, but it cannot work in such environments as the other mobile manipulators can. The others are made to work in harsh environments with limited accuracy, but their excellence is versatility. However, their payload capabilities are not suitable for various tasks.

4. MOBILE MANIPULATOR STABILITY MONITORING

Different methods for stability monitoring have been proposed in literature. One of the most used method [62] is called Zero-Moment Point (ZMP) which gives a point on the ground where moments due to external and inertial forces are in balance and the resultant is zero. Other popular methods are Force-Angle (FA) from [63] and Moment-Height Stability (MHS) from [64]. Most recent paper in the field of stability monitoring gives explicit expressions for normal wheel loads in the general case of a 4-wheeled mobile manipulator and proposes switching the paradigm from monitoring the overturning moments to monitoring normal wheel loads which should present the more efficient approach.

In this thesis, stability monitoring is done with methods described in [66] by Romanello. This method doesn't consider dynamic forces as method in [65], but only forces due to gravity. The method gives reaction forces between ground and wheels in static situation, and therefore it is not suitable for applications with high dynamic forces.

4.1 Reaction forces

Reaction forces for structure with arbitrary number of supports can be calculated using rigid body theory and the methods described [66]. With this method, all the forces must be in Z-direction.

$$\begin{cases} \sum_{i=1}^n F_i = 0 \\ \sum_{i=1}^n F_i \cdot x_i = 0 \\ \sum_{i=1}^n F_i \cdot y_i = 0 \end{cases} \quad (4.1)$$

The linear system of equations becomes statically indeterminate when there are over three unknowns but only three equations. This method uses linear elasticity of the ground to calculate the support forces. The ground is under deformation when force is applied. The displacement of the support is marked with letter z_i and the elastic constant of the ground is K^2 . The ground behaves like a spring therefore the force is the product of the elastic constant and the displacement:

$$F_i = -K^2 z_i. \quad (4.2)$$

The structure is assumed to be rigid, therefore the supports lay on the same plane after deformation. This means that the deformation z_i must satisfy the linear equation

$$z_i = ax_i + by_i + c. \quad (4.3)$$

Substituting Eq. (4.2) in Eq. (4.3), we obtain:

$$F_i = -K^2(ax_i + by_i + c). \quad (4.4)$$

To simplify the forth coming equations we introduce following equations.

$$W = \sum_{i=1}^n x_i^2 \quad (4.5)$$

$$U = \sum_{i=1}^n x_i \cdot y_i \quad (4.6)$$

$$Z = \sum_{i=1}^n y_i^2 \quad (4.7)$$

$$x_G = \frac{1}{n} \sum_{i=1}^n x_i \quad (4.8)$$

$$y_G = \frac{1}{n} \sum_{i=1}^n y_i \quad (4.9)$$

Using Eqs. (4.4) – (4.9) and the rigid body theory, we obtain:

$$\begin{cases} K^2 \cdot a \cdot W + K^2 \cdot b \cdot U + 4K^2 \cdot c \cdot x_G = -x_{Ptot} \cdot Ptot \\ K^2 \cdot a \cdot U + K^2 \cdot b \cdot Z + 4K^2 \cdot c \cdot y_G = -y_{Ptot} \cdot Ptot \\ 4K^2 \cdot a \cdot x_G + 4K^2 \cdot b \cdot y_G + 4K^2 \cdot c = -Ptot \end{cases} \quad (4.10)$$

The first row of the equation represents the moments about the x-axis, the second row represents the moments about the y-axis and the last row is the sum of the forces in z-direction. [66] The moments caused by external forces or inertia of the components can be considered by adding the moments caused by them to the first two rows of the equation (4.10). In addition, the force component in z-direction must be added to the last row of the equation. In this case, the force components must be aligned with base coordinate system. According to [66], with simple matrix calculus we can find the unknowns a, b and c.

$$AX = B \rightarrow X = A^{-1}B \quad (4.11)$$

$$A = \begin{bmatrix} W & U & 4x_G \\ U & Z & 4y_G \\ 4x_G & 4y_G & 4 \end{bmatrix} \quad (4.12)$$

$$B = \begin{bmatrix} -P_{tot} \cdot x_{P_{tot}} \\ -P_{tot} \cdot y_{P_{tot}} \\ -P_{tot} \end{bmatrix} \quad (4.13)$$

$$X = \begin{bmatrix} a \\ b \\ c \end{bmatrix} \quad (4.14)$$

Finally, we can calculate the support forces by substituting a, b and c to Eq. (4.4). [66]

In his paper [66], Romanello describes methods to calculate the support forces graphically and introduces complete support pattern (CSP) that is valid in static situation. When all supports are under force the structure is fully stable and the CoG is inside the CSP as shown in Figure 18. If the CoG is outside the CSP but inside the support pattern (SP), one of the supports is not touching the ground and the calculated support force is negative. The support with zero or negative force is at the opposite corner compared to the coordinates of the CoG. The structure is unstable if the CoG goes over one of the vertices of the SP. [66]

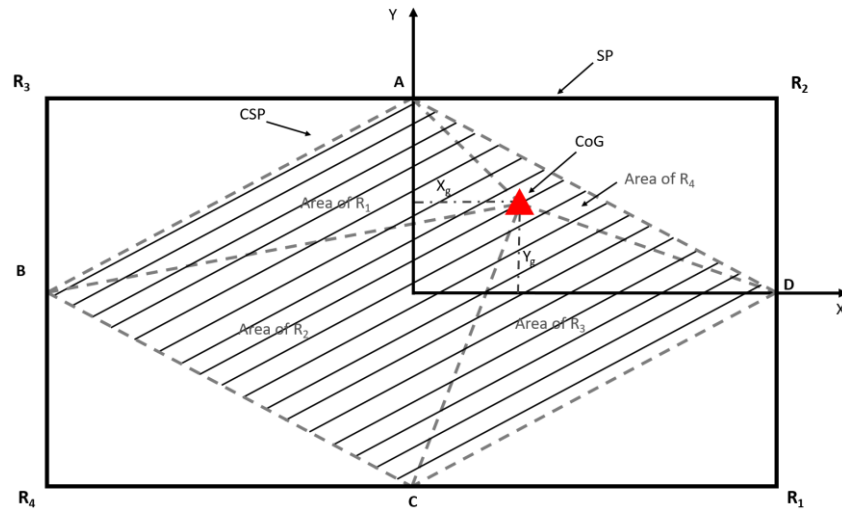


Figure 18. Graphical presentation of the CSP and SP.

The CoG divides the area of the CSP into four sections as shown with dashed lines in Figure 18. Force acting on supports R_1 to R_4 can be calculated with equations:

$$F_1 = \frac{A_{CoG-A-B} \cdot P_{tot}}{A_{tot}},$$

$$F_2 = \frac{A_{CoG-B-C} \cdot P_{tot}}{A_{tot}},$$

$$F_3 = \frac{A_{CoG-C-D} \cdot P_{tot}}{A_{tot}},$$

$$F_4 = \frac{A_{CoG-D-A} \cdot P_{tot}}{A_{tot}},$$

where A_{tot} is the area $A_{A-B-C-D}$ and other areas are triangles with hatched areas and dashed borders shown in Figure 18. If the CoG is outside the CSP, one support force is negative, but the forces can be balanced with simple math. The support that has negative value is zeroed by adding absolute value of that negative value to it. Then the value is added to the support that is in diagonally opposite direction. Then the same value is subtracted from the other supports. [66]

4.2 Stability margins and tipping angles

When the position of the CoG is calculated online, the distances to the tip-over axes and the stability angles can be calculated. The distances to the tip-over axes can be calculated with simple math if the positions of the supporting points are known. Using the well-known equation for distance between point and a line, the stability margin SM_i can be written as:

$$SM_i = \frac{|(x_i - x_{i-1}) \cdot (y_{i-1} - y_g) - (y_i - y_{i-1}) \cdot (x_{i-1} - x_g)|}{\sqrt{(x_i - x_{i-1})^2 + (y_i - y_{i-1})^2}}, \quad (4.19)$$

where the x-coordinate and y-coordinate of the CoG are x_g and y_g , respectively. The tipping angle θ_c can be calculated with equation:

$$\theta_c = \tan^{-1} \left(\frac{SM_i}{z_g} \right), \quad (4.20)$$

where z_g is the z-coordinate of the CoG.

The coordinates of CSP can be formed using methods described in [66]. As mentioned before, the CSP describes a region in which one of the reaction forces is zero and others are positive. The number of sides of the CSP is equal to the number of supporting points and therefore each of them are connected to the supporting point in the opposite direction. Equation for the coordinates of the CSP can be written as:

$$[x_i \ y_i \ 1] = \mathbf{A}_i \cdot \begin{bmatrix} x \\ y \\ 1 \end{bmatrix} = 0, \quad (4.21)$$

where x_i and y_i are the location of the supporting points and \mathbf{A}_i is the matrix from Eq. (4.12).

5. SIMULATION RESULTS

The simulation model for the mobile manipulator is presented in Appendix D. The mobile manipulator's TCP is instructed to follow the path along cartesian axes X, Y and Z shown in Figure 19 below. At the same time various signals are monitored.

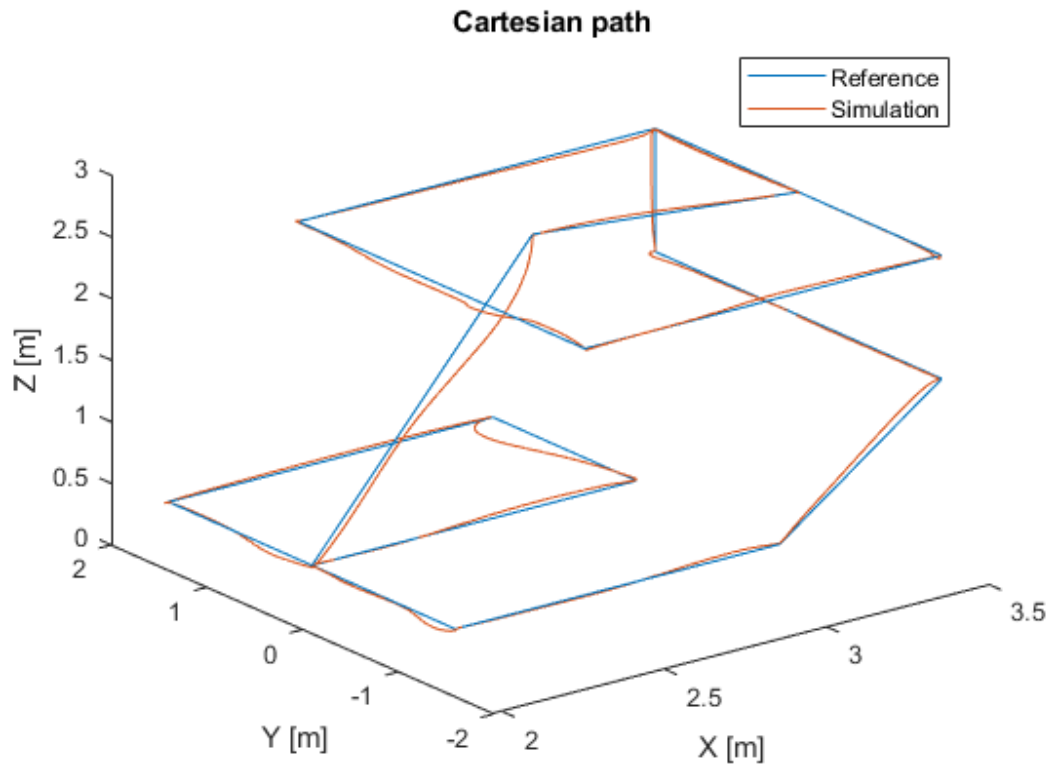


Figure 19. Reference end-effector path and simulated path.

As can be seen in Figure 19, there is some error between the reference path and simulated path. This is due to that some of the joints go to their limits or the reference points are unattainable in this position. References, measured positions and maximum errors of the joint angles are shown in Figure 20.

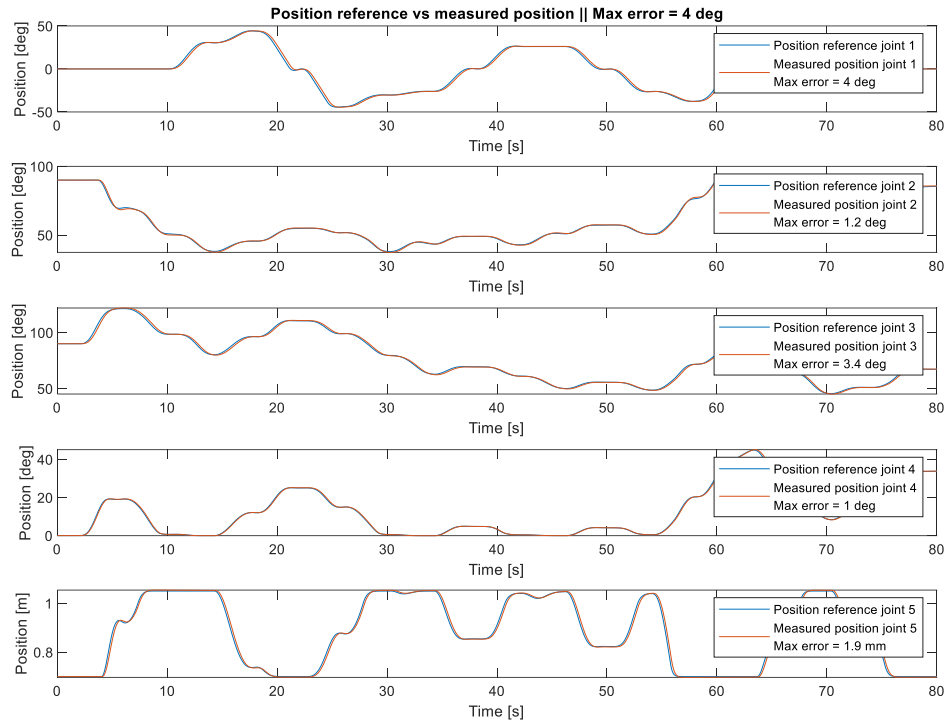


Figure 20. Position references, measured positions and maximum errors for all joints.

As can be seen from the figure above, the manipulator cannot follow the reference at some points, which causes error. The controller structure and implementation fall out of the scope of this thesis. Therefore, the implemented controller has simple PI structure and it is used to approximately achieve the required manipulator postures. Using the implemented controller, a perfect reference tracking cannot be achieved, but it entirely suffices for the underlying analysis.

5.1 Manipulator's actuator forces and velocities

Mobile manipulator's actuator forces and velocities can be obtained from the MATLAB Simscape Multibody model. This data can be used to dimension the EMLAs. At the beginning when the gear ratios and other parameters are unknown, actuator position can be fed into simulation model to obtain estimates for the actuator forces and velocities. Next, the EMLAs can be dimensioned using this data. After the EMLAs parameters are chosen, controller, motor and mechanical model can be added to simulation model. These components introduce oscillation as the actuators act like springs with high stiffness. The simulation models are shown in Appendix D. The forces, velocities and powers shown in Figure 21 are obtained when the manipulator is guided along the path shown in Figure 19.

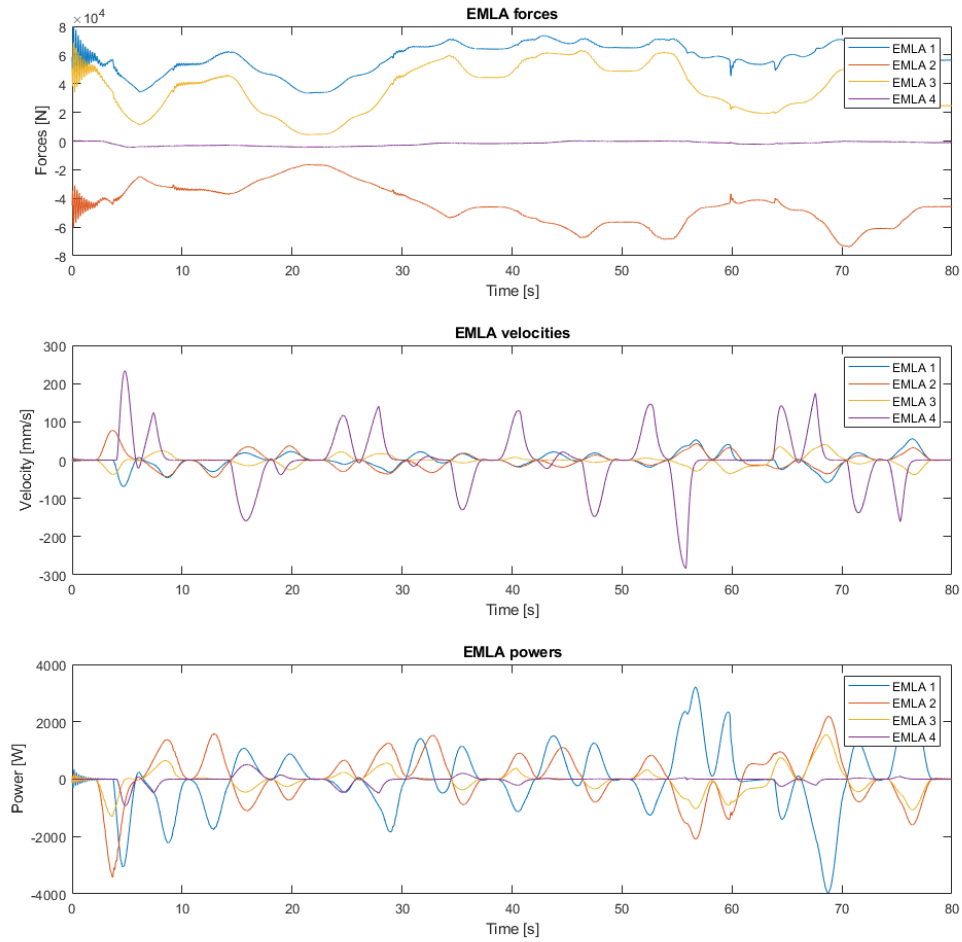


Figure 21. Actuator forces, velocities and powers of the EMLAs.

As can be seen from the Figure 21, at the start of the simulation the manipulator begins to oscillate. This is due to that there is no gravity compensation in the controller therefore it takes some time for motors to generate torque for EMLAs.

The fatigue lives of the ball screws can be calculated using the data from the simulation and the process from chapter 2.2.2. Calculated fatigue lives are for example purposes only as they are calculated from the same data as other results. The manipulation is performed with maximum load that the mobile manipulator can manage to move along the path in Figure 19 without overturning. Therefore, the calculated fatigue lives are lower than in normal operation. The specification for ball screw used with all the EMLAs can be found from Table 6. The ball screws have dynamic load rating of 79700 kN. The results are shown in Table 5.

Table 5. Calculated fatigue lives of EMLAs.

Calculated value	EMLA 1	EMLA 2	EMLA 3	EMLA 4
Maximum force F_{max}	82,6 kN	73,8 kN	−68,9 kN	−4,3 kN
Equivalent dynamic axial load F_m	63,3 kN	54,8 kN	−44,2 kN	2,0 kN
Maximum linear velocity V_{max}	69,2 mm/s	77,8 mm/s	40,5 mm/s	273,2 mm/s
Average revolutions per minute N_m	70,3 RPM	66,3 RPM	49,7 RPM	205 RPM
Fatigue life L_{10}	$2,0 \cdot 10^6$ revs	$3,1 \cdot 10^6$ revs	$5,9 \cdot 10^6$ revs	$6,5 \cdot 10^{10}$ revs
Fatigue life L_{km}	20,0 km	30,8 km	58,6 km	646,5 tkm

As can be seen in Table 5, fatigue lives in kilometers are the lowest for the EMLA 1 since the equivalent dynamic axial load and average revolutions have highest values. On the other hand, EMLA 4 has highest fatigue life because the forces are much smaller compared to others.

5.2 Manipulator's natural frequencies

Manipulator's natural frequencies are difficult to determine without simulation if there are several joints. On the other hand, simulation gives natural frequencies only in the position in which the manipulator is simulated. Analytical calculations can provide the natural frequencies in any posture, but the results require complex calculations. Figure 22 presents the natural frequencies in position where the joints are at: 0° , 90° , 90° , 0° and 0,7 m.

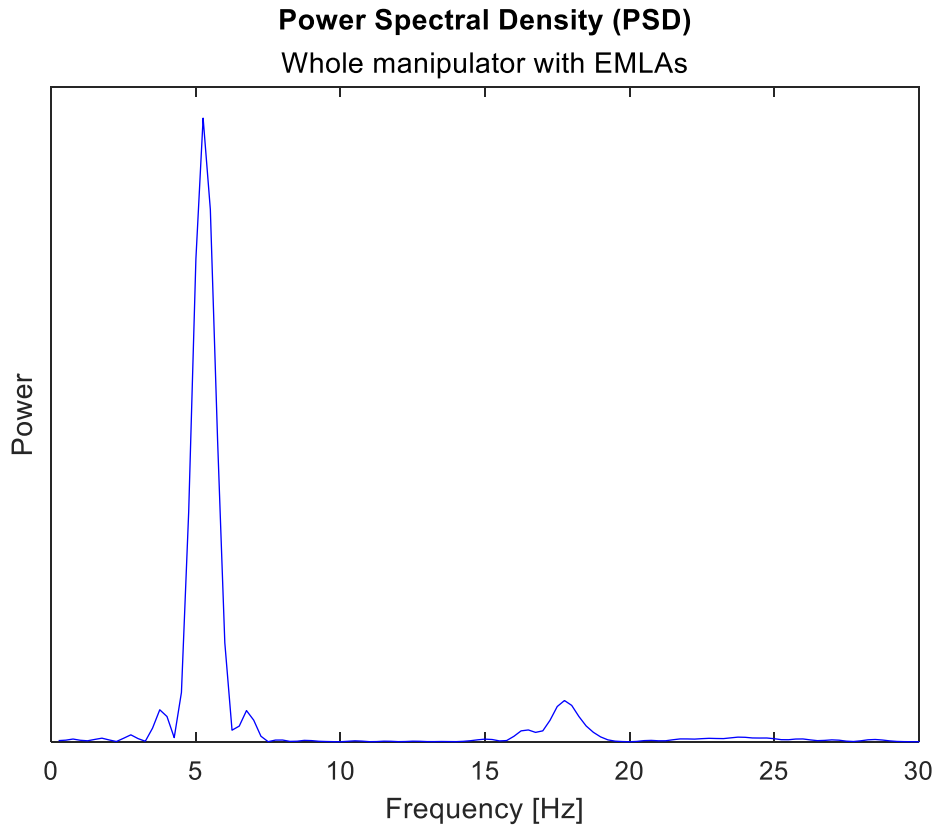


Figure 22. *Natural frequencies of the manipulator.*

Comparison between the hydraulic cylinder and the EMLA are done by comparing the lowest natural frequency in 1-DOF case because analytic results for this kind of structure requires complex calculations. This is done by comparing the actuator of the 3rd joint and assuming that the other actuators are rigid. This means that the natural frequency depends only on the stiffness of the actuator, moment arm and the inertia of the structure after the 3rd joint. Simplified figure of the posture and oscillation directions are shown in Figure 23.

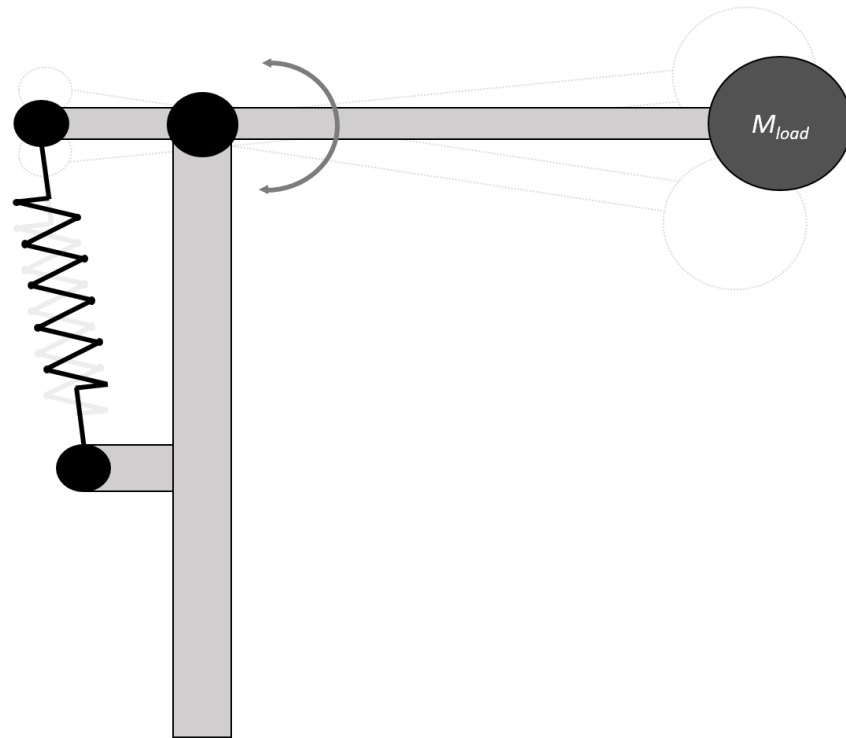


Figure 23. Manipulator posture and oscillation directions.

The light color lines in Figure 23 shows the oscillation in the manipulator. The amplitude of the oscillation is exaggerated for illustrative purposes. Parameters for calculating the stiffness of the hydraulic cylinder are shown below. Bulk modules of the pipes or hoses are neglected.

Table 6. Parameters for hydraulic cylinder.

Parameter	Hydraulic cylinder
Piston area	$A_{piston} = 5000 \text{ mm}^2$
Piston rod area	$A_{rod} = 3400 \text{ mm}^2$
Stroke	$L_{hc} = 358 \text{ mm}$
Bulk modulus of the fluid	$B = 1200 \text{ MPa}$
Dead volume (both ends)	$V_d = 0,3 \text{ l}$

The EMLA requires more parameters to calculate stiffness compared to the hydraulic cylinder. These parameters are also included in the simulation model. Parameters for EMLA are shown in Table 7.

Table 7. Parameters for EMLA.

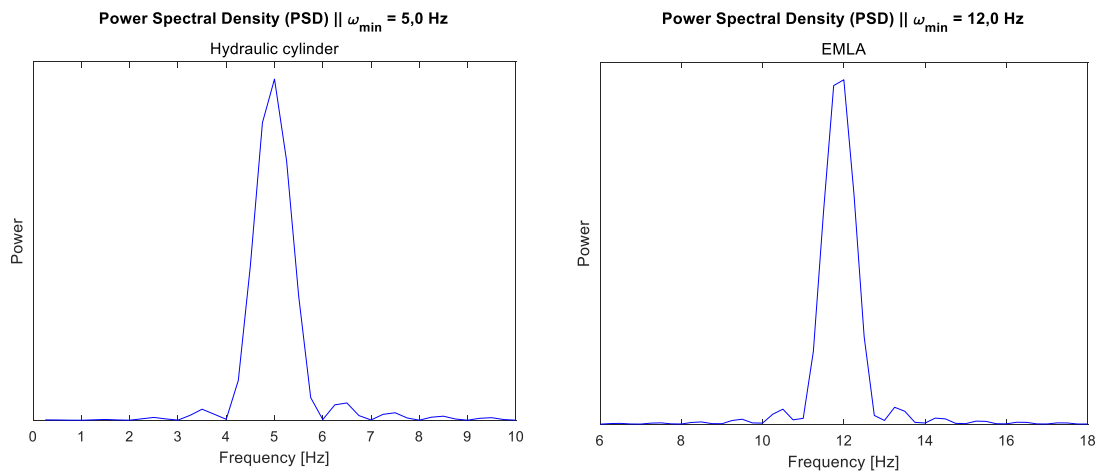
Parameter	EMLA
Nominal diameter	$D_{nom} = 50 \text{ mm}$
Lead of the ball screw	$p_{bs} = 10 \text{ mm}$
Dead length of the screw	$L_{dl} = 104,5 \text{ mm}$
Ball diameter	$d_w = 6 \text{ mm}$
Cross-sectional diameter	$V_d = 45,7 \text{ mm}$
Thrust tube inner diameter	$D_{rod} = 55 \text{ mm}$
Thrust tube outer diameter	$D_{rod} = 110 \text{ mm}$
Thrust tube length	$L_{rod} = 358 \text{ mm}$
Thrust tube stiffness	$R_{rod} = 426,6 \frac{\text{N}}{\text{ym}}$
Ball screw nut stiffness	$R_{nut} = 1065,4 \frac{\text{N}}{\text{ym}}$
Bearing stiffness	$R_b = 1470 \frac{\text{N}}{\text{ym}}$

Apart from the constant stiffness parameters, ball screws axial and radial stiffnesses depends on the nut position and they are calculated with equations presented in section 2.2.3. Natural frequencies of the oscillating arm can be calculated by using the equations presented in sections 2.1 and 2.2. Table 8 shows the general parameters for calculating the natural frequencies and the results for both actuators. The inertia of the load mass, arm and dimensions are obtained from CAD-file. The moment arm is calculated from the geometry using the equations from Appendix A.

Table 8. Calculated parameter and natural frequencies.

Parameter	Hydraulic cylinder 80x45x358	EMLA 50x10x358
Inertia of the load mass and arm	$J_{ma} = 2601,8 \text{ kgm}^2$	$J_{ma} = 2601,8 \text{ kgm}^2$
Moment arm	$r = 249 \text{ mm}$	$r = 249 \text{ mm}$
Stiffness of the actuator	$KH_{tot} = 40,3 \frac{\text{N}}{\gamma\text{m}}$	$R_{tot} = 231,7 \frac{\text{N}}{\gamma\text{m}}$
Natural frequency	$f_{AR,H} = 5,0 \text{ Hz}$	$f_{AR,E} = 11,9 \text{ Hz}$

Table 8 shows differences between hydraulic cylinder and EMLA. Hydraulic cylinders stiffness is under 20 % of stiffness of EMLA because the fluid is highly compressible. This has direct connection to the natural frequency of the manipulator and therefore the natural frequency of the EMLA is over twice as high as the hydraulic cylinder's natural frequency. Calculated natural frequency can be verified by simulation in Simulink. This can be done by giving an impulse excitation to the manipulator. This causes the manipulator to start oscillating at its own natural frequency. Then the signals can be measured from the simulation and the Power Spectral Density (PSD) can be estimated using MATLAB. Natural frequencies obtained from the simulation are shown in Figure 24.

**Figure 24.** Natural frequencies of the hydraulic cylinder and EMLA in 1-DOF case.

As can be seen from the Figure 23, the frequencies are same as with the analytical solution.

5.3 Stability of the mobile manipulator

Stability monitoring can be included in the simulation model. Monitoring can be done by observing the reaction forces between the ground and wheels or calculating the stability margins or angles described in section 4.2. The reaction forces calculated from the simulation are shown in Figure 25.

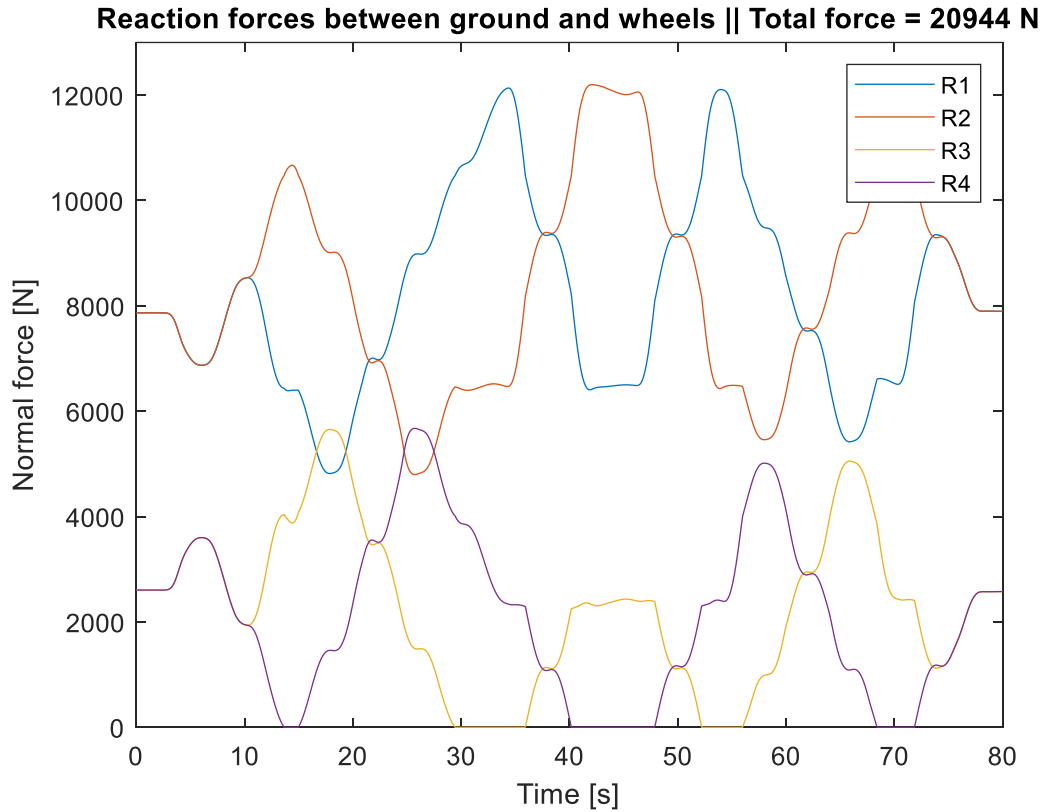


Figure 25. Reaction forces for the four wheels.

The reaction forces in the Figure 25 have been calculated using the equations from chapter 4.1. The reaction forces are calculated from the simulation data as the manipulator's end-effector travels along the path of Figure 19. Calculated reaction forces ignore inertial forces which can be substantial in high velocity applications. Reaction forces can be used to prevent the mobile manipulator from overturning which is essential for mobile machinery. As can be seen from Figure 25, rear wheel forces go to zero on the rear wheels at several points which means that the CoG goes over the CSP described in section 4. At these points, the mobile manipulator is in danger of overturning therefore the movements of the manipulator should be stopped or slow down to ensure the stability.

6. CONCLUSIONS

In this thesis, conceptual design of mobile manipulator was presented and simulation model for the mobile manipulators was developed including mechanical models for actuators and stability monitoring features. The theoretical sections of this thesis are divided into three different subject areas, the first of which gives an overview of hydraulic cylinders and electromechanical linear actuators, the second which discusses the differences and limitations of industrial robots and mobile manipulators and the last that summarizes the importance of stability monitoring of mobile manipulators and presents a way to prevent the mobile manipulator from overturning. The methods in the theoretical part are combined and brought into the simulation model which is used to simulate the mobile manipulator and to study the properties of hydraulic and electric actuators and the stability of the mobile manipulator.

The simulation has been found to be a great tool in the sizing of actuators, as it can produce more accurate data from the simulated movements of the manipulator compared to estimated work cycles. It is possible to obtain information about the forces and velocities of the actuators by giving the joints only motion inputs. Based on the data obtained from these simulations, it is possible to dimension EMLAs and build a more realistic model with controllers and EMLAs that incorporate their mechanical properties. If the work cycles of the manipulator are known, the simulations can also be used to determine the service life and service intervals of EMLAs. In addition, the simulation model provides a platform to test and tune the controllers and build a realistic digital twin.

A hydraulic cylinder and an EMLA have different kind of structures which affects their dynamic performances. The results show that manipulators with EMLAs have higher natural frequencies which affect the performance of the manipulator. EMLAs can provide an alternative for hydraulic actuators in different applications as they are stiffer and more accurate than conventional hydraulic cylinders. In addition, they are more environmentally friendly which is important today, and therefore many manufacturers are interested on electric alternatives.

The performance of the mobile manipulator would have been improved if there was more time to concentrate on detailed modelling of the mobile manipulator. The dimensions of the mobile manipulator are important as the EMLAs require more space compared to hydraulic cylinders. Better designed dimensions would have allowed for a larger work area. In addition, algorithms for limiting the movements of the joints should have been

implemented to prevent the joints reaching the limits during manipulation. Besides these, better selection of the motors or restricting the joint velocities would have improved reference tracking. The future work should include tests in a real system to verify the differences between hydraulic cylinders and EMLAs. This is needed as the electric alternatives are becoming the future.

REFERENCES

- [1] J. M. Ratzinger, S. Buchberger, and H. Eichlseder, "Electrified powertrains for wheel-driven non-road mobile machinery," *Automot. Engine Technol.*, vol. 6, no. 1–2, pp. 1–13, 2021, doi: 10.1007/s41104-020-00072-z.
- [2] D. Vandenbroucke, A. Van Hyfte, and L. Franckx, "Study in View of the Revision of Directive 97/68/EC on Non-Road Mobile Machinery (NRMM) (Module I - An Emissions Inventory)," no. December, 2010, [Online]. Available: <https://op.europa.eu/en/publication-detail/-/publication/60e67ef3-f68f-42d0-ba3f-afb053704359/language-en/format-PDF/source-239062641>.
- [3] International Energy Agency, "Trends and developments in electric vehicle markets – Global EV Outlook 2021 – Analysis - IEA," *IEA.org*, 2021. <https://www.iea.org/reports/global-ev-outlook-2021/trends-and-developments-in-electric-vehicle-markets> (accessed Oct. 29, 2021).
- [4] Volvo Construction Equipment, "Volvo CE unveils 100 percent electric compact excavator prototype: Volvo Construction Equipment," 2017. <https://www.volvoce.com/global/en/news-and-events/press-releases/2017/volvo-ce-unveils-100-percent-electric-compact-excavator-prototype/> (accessed Oct. 29, 2021).
- [5] Yanmar, "Yanmar Unveils its Exciting New eFuzion Concept at bauma," 2019. <https://www.yanmar.com/global/construction/news/2019/04/10/53748.html> (accessed Oct. 29, 2021).
- [6] Bobcat, "T7X All-Electric Compact Track Loader," 2022. <https://www.bobcat.com/company-info/innovation/all-electric-compact-loader> (accessed May 16, 2022).
- [7] L. Zhang *et al.*, "An autonomous excavator system for material loading tasks," *Sci. Robot.*, vol. 6, no. 55, pp. 1–13, 2021, doi: 10.1126/scirobotics.abc3164.
- [8] Sandvik AB, "Sandvik pushes the boundaries of mining automation with the reveal of its AutoMine Concept." <https://www.rocktechnology.sandvik/en/news-and-media/news-archive/2020/09/sandvik-pushes-the-boundaries-of-mining-automation-with-the-reveal-of-its-automine-concept/> (accessed Nov. 04, 2021).
- [9] A. Akers, M. Gassman, and R. Smith, "Hydraulic power system analysis." pp. 1–366, 2006, doi: 10.1201/9781420014587.
- [10] H. McCoy, "US2366739A - Electrical jack - Google Patents," 1945. <https://patents.google.com/patent/US2366739A/en> (accessed Nov. 02, 2021).
- [11] LINAK, "The history of LINAK – From the first linear actuator to worldwide market leader," *linak.co.uk*, 2020. <https://www.linak.com/about-linak/history/> (accessed Nov. 02, 2021).
- [12] H. Kauranne, J. Kajaste, and M. Vilenius, "Hydrauliteknikka." Sanoma Pro, Helsinki, p. 496, 2013.

- [13] M. Linjama, "Puomin dynamiikkaan vaikuttavat tekijät," 1996, p. 34.
- [14] J. Watton, "Fundamentals of Fluid Power Control." Cambridge University Press, New York, pp. 1–494, 2009, doi: 10.1017/CBO9781139175241.
- [15] M. Linjama, "Lecture 5: Dimensioning hydraulic servo systems [PowerPoint slides]," in *IHA-2506 Control of Hydraulic Actuators*, Faculty of Engineering and Natural Sciences, Tampere University, 2021.
- [16] Design World Staff, "Roller Screw Actuators: Benefits, Selection and Maintenance," 2010. <https://www.designworldonline.com/roller-screw-actuators-benefits-selection-and-maintenance/> (accessed Nov. 10, 2021).
- [17] Enrgtech, "ET13886820 | XCT20x4M w/F75 | Thomson Linear XCT20x4M w/F75 Flanged Anti-Backlash Nut For Lead Screw, Dia. 20mm." <https://www.enrgtech.co.uk/buy/product/ET13886820/XCT20x4M-w-F75> (accessed Nov. 10, 2021).
- [18] Drivelines, "What's the difference between a ball screw and a lead screw?," 2020. <https://drivelines.co.uk/2020/02/04/ball-lead-screw/> (accessed Nov. 10, 2021).
- [19] Y. Dhaware, P. Palkuntwar, H. Narkhede, R. Meher, P. Chavan, and B. Gandevia, "Review on Comparative Analysis of Ball Screw & Lead Screw," no. June, pp. 769–772, 2019.
- [20] P. C. Lemor, "Roller screw, an efficient and reliable mechanical component of electro-mechanical actuators," in *Proceedings of the Intersociety Energy Conversion Engineering Conference*, 1996, vol. 1, pp. 215–220, doi: 10.1109/iecec.1996.552873.
- [21] S. Ma, T. Zhang, G. Liu, R. Tong, and X. Fu, "Kinematics of Planetary Roller Screw Mechanism considering Helical Directions of Screw and Roller Threads," *Math. Probl. Eng.*, vol. 2015, 2015, doi: 10.1155/2015/459462.
- [22] S. Ma, G. Liu, R. Tong, and X. Fu, "A Frictional Heat Model of Planetary Roller Screw Mechanism Considering Load Distribution," *Mech. based Des. Struct. Mach.*, vol. 43, no. 2, pp. 164–182, 2015, doi: 10.1080/15397734.2014.938816.
- [23] Ewellix, "Ewellix part of NASA's Mission Mars 2020!" <https://www.ewellix.com/en/cn/newsroom/ewellix-part-nasas-mission-mars-2020> (accessed Nov. 11, 2021).
- [24] S. Shimizu, H. Shimoda, and C. S. Sharma, "Re-evaluation of basic dynamic load rating and life formula for a ball screw," *Tribol. Trans.*, vol. 50, no. 1, pp. 88–95, 2007, doi: 10.1080/10402000601105599.
- [25] ISO, "ISO 3408-5:2006, Ball screws — Part 5: Static and dynamic axial load ratings and operational life." p. 14, 2006.
- [26] D. Collins, "Ball screw standards: Differences between DIN, ISO, and JIS." <https://www.linearmotiontips.com/ball-screw-standards-what-you-need-to-know-about-din-iso-and-jis/> (accessed Nov. 12, 2021).
- [27] R. L. Norton, "Machine design: an integrated approach." Pearson Education, Hoboken, N.J, 2020.

- [28] S. P. Timoshenko, "Theory of Elastic Stability." Dover Publications, Newburyport, 2012.
- [29] R. Lakshmipathy, "Nonlinear buckling with no penetration contact support in 2017," 2016. <https://blogs.solidworks.com/tech/2016/09/nonlinear-buckling-no-penetration-contact-support-2017.html> (accessed Nov. 15, 2021).
- [30] D. Collins, "What is ball screw whip and why does it happen?," 2021. <https://www.linearmotiontips.com/what-is-ball-screw-whip-and-why-does-it-happen/> (accessed Nov. 16, 2021).
- [31] NSK, "Ball screws." https://stevenengineering.com/Tech_Support/NSK.htm (accessed Nov. 16, 2021).
- [32] ISO, "ISO 3408-4:2006, Ball screws — Part 4: Static axial rigidity." p. 18, 2006.
- [33] MITCalc, "Ball screws." https://www.mitcalc.com/en/pr_ball screws.htm (accessed Nov. 18, 2021).
- [34] J. Sobolewski, "Some Remarks on the Ball Screw Rigidity," *Mach. Dyn. Probl.*, vol. 30, no. 4, pp. 122–130, 2006.
- [35] R. Caracciolo and D. Richiedei, "Optimal design of ball-screw driven servomechanisms through an integrated mechatronic approach," *Mechatronics*, vol. 24, no. 7, pp. 819–832, 2014, doi: 10.1016/j.mechatronics.2014.01.004.
- [36] K. Wang, C. G. Zhou, and Y. Ou, "Investigation of the fluctuation of the static axial rigidity for double-nut preloaded ball screws," *Adv. Mech. Eng.*, vol. 11, no. 1, pp. 1–9, 2019, doi: 10.1177/1687814018822181.
- [37] D. Collins, "What is preload?," 2015. <https://www.linearmotiontips.com/a-users-guide-to-preload/> (accessed Nov. 24, 2021).
- [38] K. Chen, L. Zu, and L. Wang, "Prediction of preload attenuation of ball screw based on support vector machine," *Adv. Mech. Eng.*, vol. 10, no. 9, p. 168781401879916, 2018, doi: 10.1177/1687814018799161.
- [39] G. Qiao, G. Liu, Z. Shi, Y. Wang, S. Ma, and T. C. Lim, "A review of electromechanical actuators for More/All Electric aircraft systems," *Proc. Inst. Mech. Eng. Part C J. Mech. Eng. Sci.*, vol. 232, no. 22, pp. 4128–4151, 2018, doi: 10.1177/0954406217749869.
- [40] J.-C. Maré, "Aerospace actuators 2: signal-by-wire and power-by-wire," *Aerospace Actuators 2*, vol. 2, no. April 1992. ISTE, London, p. 217, 2017.
- [41] I. Ansoategui and F. J. Campa, "Mechatronics of a ball screw drive using an N degrees of freedom dynamic model," *Int. J. Adv. Manuf. Technol.*, vol. 93, no. 1–4, pp. 1307–1318, 2017, doi: 10.1007/s00170-017-0597-2.
- [42] G. Ellis, "Control System Design Guide," *Control System Design Guide*. Elsevier Academic Press, Amsterdam, 2012, doi: 10.1016/C2010-0-65994-3.
- [43] I. Zamalloa, R. Kojcev, and A. Hern, "Dissecting Robotics — historical overview and future perspectives," pp. 1–9, 2017.
- [44] O. Holland, "The first biologically inspired robots," *Robotica*, vol. 21, no. 4, pp.

- 351–363, 2003, doi: 10.1017/S0263574703004971.
- [45] Robotnik, “History of Robots and Robotics.” p. 1, 2021, Accessed: Dec. 01, 2021. [Online]. Available: <https://robotnik.eu/history-of-robots-and-robotics/>.
 - [46] A. Marzoughi, “Collision Free Navigation of a Multi-Robot Team for Intruder Interception,” no. November. Sep. 07, 2018, doi: 10.13140/RG.2.2.34721.86889.
 - [47] SRI International, “Shakey the Robot,” 2018. <https://www.sri.com/hoi/shakey-the-robot/> (accessed Dec. 01, 2021).
 - [48] NASA, “Lunokhod 01,” 2018. <https://solarsystem.nasa.gov/missions/lunokhod-01/in-depth/> (accessed Dec. 01, 2021).
 - [49] A. Gasparetto and L. Scalera, “A Brief History of Industrial Robotics in the 20th Century,” *Adv. Hist. Stud.*, vol. 08, no. 01, pp. 24–35, 2019, doi: 10.4236/ahs.2019.81002.
 - [50] G. Mester, “Applications of Mobile Robots,” *Appl. Mob. Robot.*, no. April 2006, pp. 6–12, 2019, doi: 10.5772/intechopen.74181.
 - [51] Isak Karabegović, “Industrial Robots: Design, Applications and Technology.” Nova Science Publishers, New York, p. 461, 2020.
 - [52] ABB, “IRB 8700.” <https://new.abb.com/products/robotics/industrial-robots/irb-8700> (accessed Feb. 08, 2022).
 - [53] Fanuc, “M-2000iA / 2300.” <https://www.fanuc.eu/fr/en/robots/robot-filter-page/m-2000-series/m-2000ia-2300> (accessed Feb. 08, 2022).
 - [54] KUKA, “KR 1000 titan.” <https://www.kuka.com/en-ch/products/robotics-systems/industrial-robots/kr-1000-titan> (accessed Feb. 08, 2022).
 - [55] A. Kivila, “Modeling, estimation and control for serial flexible robot arms,” Georgia Institute of Technology, 2017.
 - [56] Z. Li, “Fundamentals in modeling and control of mobile manipulators.” CRC Press, Boca Raton, 2013.
 - [57] KUKA, “KMR QUANTEC,” 2016. <https://www.kuka.com/en-de/products/mobility/mobile-robots/kmr-quantec> (accessed Feb. 14, 2022).
 - [58] KUKA, “KUKA KMR QUANTEC datasheet,” 2021. <https://www.kuka.com/en-de/services/downloads?terms=Language:en:1&q=> (accessed Mar. 23, 2022).
 - [59] L3HARRIS, “T7™ Multi-Mission Robotic System.” <https://www.l3harris.com/all-capabilities/t7-multi-mission-robotic-system> (accessed Mar. 23, 2022).
 - [60] Telerob, “Telerob tEODor EVO,” 2020. <https://www.telerob.com/en/news-media/pictures> (accessed Mar. 23, 2022).
 - [61] K. Berns, A. Nezhadfar, M. Tosa, H. Balta, and G. De Cubber, “Unmanned Ground Robots for Rescue Tasks,” in *Search and Rescue Robotics - From Theory to Practice*, IntechOpen, 2017.
 - [62] M. Vukobratović and B. Borovac, “Zero-Moment Point — Thirty five years of its

- life," *Int. J. Humanoid Robot.*, vol. 1, no. 1, pp. 157–173, 2004, doi: 10.1142/S0219843604000083.
- [63] E. Papadopoulos and D. A. Rey, "The Force-Angle Measure of Tipover Stability Margin for Mobile Manipulators," *Veh. Syst. Dyn.*, vol. 33, no. 1, pp. 29–48, 2000, doi: 10.1076/0042-3114(200001)33:1;1-5;FT029.
 - [64] S. A. A. Moosavian and K. Alipour, "On the dynamic tip-over stability of wheeled mobile manipulators," *Int. J. Robot. Autom.*, vol. 22, no. 4, pp. 322–328, 2007, doi: 10.2316/journal.206.2007.4.206-3036.
 - [65] G. R. Petrović and J. Mattila, "Analytic Solutions for Wheeled Mobile Manipulator Supporting Forces," pp. 1–19, 2022.
 - [66] G. Romanello, "A graphical approach for the determination of outrigger loads in mobile cranes," *Mech. Based Des. Struct. Mach.*, vol. 0, no. 0, pp. 1–14, 2020, doi: 10.1080/15397734.2020.1726184.
 - [67] B. Siciliano, "Robotics : modelling, planning and control." Springer, London, 2009.

APPENDIX A: LENGTH OF THE ACTUATORS AND JOINT ANGLES

The mobile manipulator has five different joints as shown in Figure A.

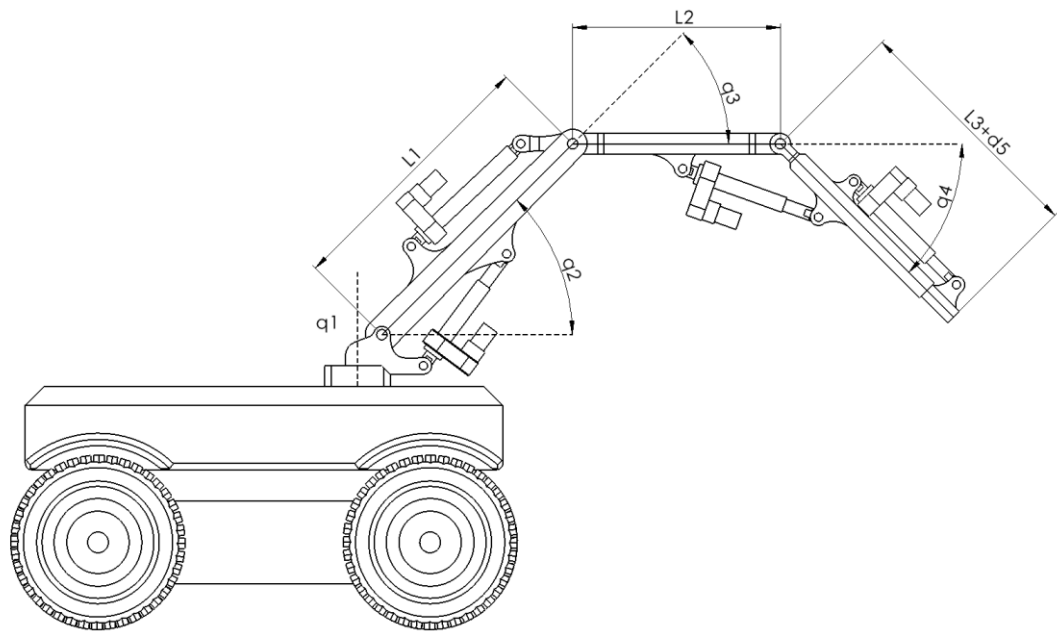


Figure A. *Mobile manipulator joint mapping.*

The mobile manipulator's arm consists of four rigid links which are actuated with EMLAs. The joint movements are positive if rotated in the counterclockwise direction. Figure B shows the relation between the actuator length Z_1 and the joint angle q_2 .

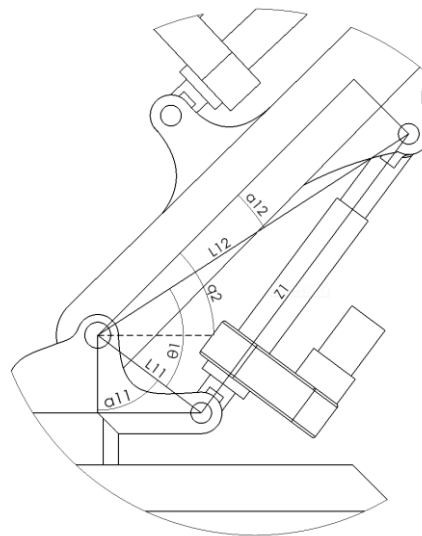


Figure B. The relation between the length of the first EMLA and the joint angles.

The actuator length Z_1 can be calculated by using the cosine law and the dimensions from the manipulator:

$$Z_1 = \sqrt{L_{11}^2 + L_{12}^2 - 2 \cdot L_{11} \cdot L_{12} \cdot \cos(\theta_1)}, \quad (\text{A. 1})$$

where

$$\theta_1 = q_2 - \alpha_{12} - \alpha_{11} + \pi/2. \quad (\text{A. 2})$$

Solving θ_1 from Eq. (A.1) and substituting the result to Eq. (A.2) the joint angle q_2 as a function of the actuator length Z_1 can be calculated with equation:

$$q_2 = \arccos\left(\frac{L_{11}^2 + L_{12}^2 - Z_1^2}{2L_{11} \cdot L_{12}}\right) + \alpha_{12} + \alpha_{11} - \pi/2. \quad (\text{A. 3})$$

The relation between the joint velocity and the actuator velocity can be obtained by differentiating Eq. (A.1):

$$r_1 = \frac{L_{11} \cdot L_{12} \cdot \cos(\theta_1)}{Z_1}, \quad (\text{A. 4})$$

where r_1 is the moment arm.

The structure of the third joint is slightly different as shown in Figure C.

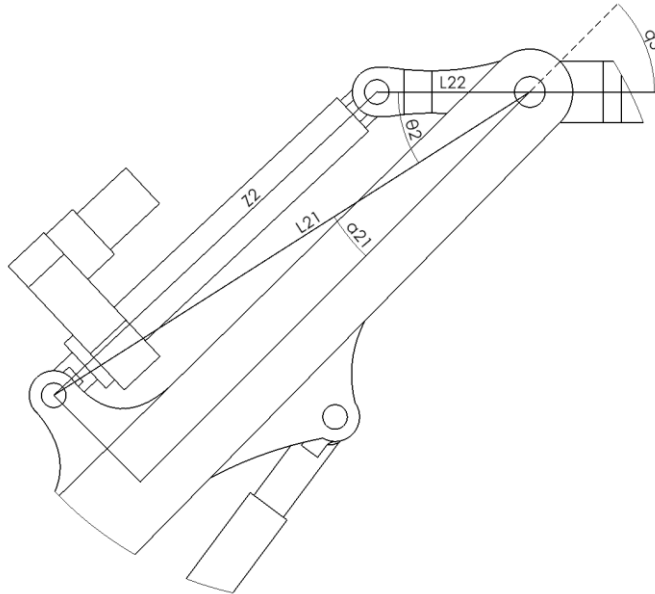


Figure C. The relation between the length of the second EMLA and joint angles.

The second EMLA is directly attached to the second link and its movement in the positive direction causes the third joint to rotate in the negative direction. The length of the actuator can be calculated with equation

$$Z_1 = \sqrt{L_{21}^2 + L_{22}^2 - 2 \cdot L_{21} \cdot L_{22} \cdot \cos(\theta_2)}, \quad (\text{A.4})$$

where

$$\theta_2 = q_3 - \alpha_{21}. \quad (\text{A.5})$$

The joint angle can be calculated using Eqs. (A.4) and (A.5):

$$q_3 = \arccos\left(\frac{L_{21}^2 + L_{22}^2 - Z_2^2}{2 \cdot L_{21} \cdot L_{22}}\right) + \alpha_{12}. \quad (\text{A.6})$$

The moment arm can be obtained similarly as in E.q. (A.4):

$$r_2 = \frac{L_{21} \cdot L_{22} \cdot \cos(\theta_2)}{Z_2}. \quad (\text{A.7})$$

The structure of the fourth joint is shown in Figure D.

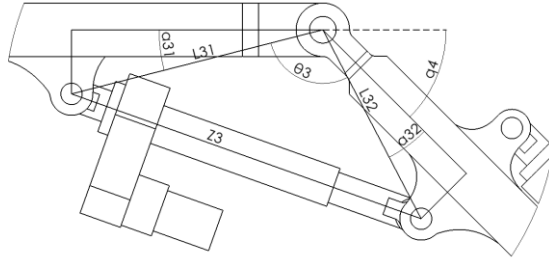


Figure D. The relation between the length of the third EMLA and joint angles.

The structure of the third joint is similar to that of the first joint. The difference between these is how the joint angle is measured. The length of the third actuator can be calculated with equation:

$$Z_3 = \sqrt{L_{31}^2 + L_{32}^2 - 2 \cdot L_{31} \cdot L_{32} \cdot \cos(\theta_3)}, \quad (\text{A.8})$$

where

$$\theta_3 = -q_4 - \alpha_{31} - \alpha_{32} + \pi. \quad (\text{A.9})$$

The joint angle q_4 can be expressed as the function of the actuator length Z_3 by using Eqs. (A.8) and (A.9):

$$q_4 = \arccos\left(\frac{L_{31}^2 + L_{32}^2 - Z_3^2}{2L_{31} \cdot L_{32}}\right) + \theta_3 + \alpha_{31} + \alpha_{32} - \pi. \quad (\text{A.10})$$

For the fourth joint, the moment arm can be expressed as:

$$r_3 = \frac{L_{31} \cdot L_{32} \cdot \cos(\theta_3)}{Z_3}. \quad (\text{A.11})$$

APPENDIX B: DH-PARAMETERS

Widely used Denavit-Hartenberg convention can be used to calculate the forward kinematics for manipulators with an open-chain structure. Transformation between two coordinate frames can be described with four parameters, three of the parameters are constant and one is variable which can be revolute q_i or prismatic d_i . [67]

Mobile manipulator has four revolute joints and one prismatic joint. First joint is actuated with rotational actuator and joints two to five are actuated with linear actuators. Last coordinate frame of the mobile manipulator is aligned with base frame when the manipulator is pointing forward. Figure E shows the coordinate frames of the mobile manipulator.

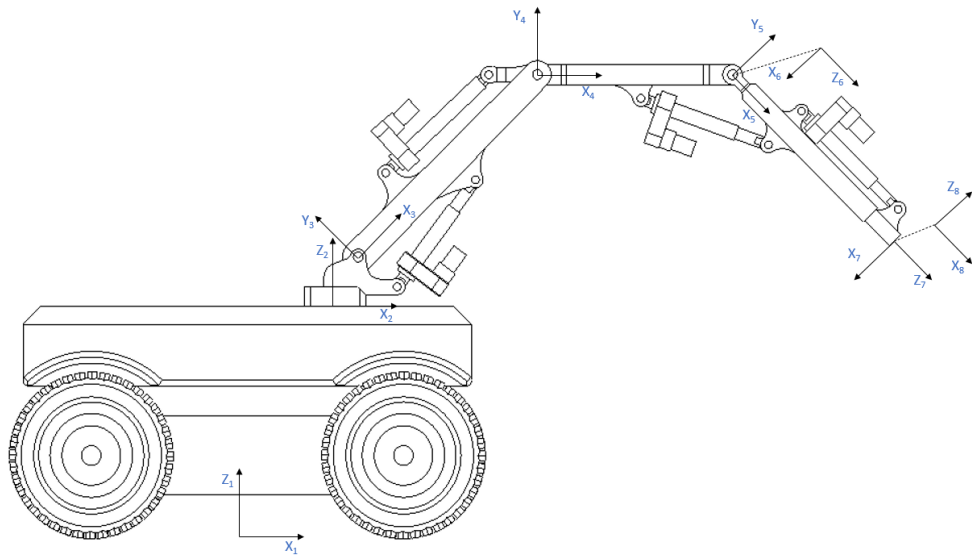


Figure E. Mobile Manipulator's coordinate frames.

The constant parameters of the DH-parameters are a_i and α_i . Parameter a_i is the length of the i :th link, d_i is the z-coordinate distance between two links, α_i is the rotation angle of x-axis between two frames. The joint variable q_i is variable angle or distance of z-axis between two frames of the i :th joint. The angles are positive if rotated counterclockwise. Table A shows the DH parameters for the mobile manipulator.

Table A. The DH-parameters for the mobile manipulator.

Frame No.	a_i	d_i	q_i	α_i
1	x1	z1	0	0
2	x2	z2	q_1	$\pi/2$
3	x3	0	q_2	0
4	x4	0	$-q_3$	0
5	0	0	$-q_3 - \pi/2$	$-\pi/2$
6	0	$x_5 + d_5$	$-\pi/2$	$\pi/2$
7	0	0	$\pi/2$	0

APPENDIX C: FORWARD KINEMATICS

Using the expressions from [67], the position and the orientation change of each coordinate frame can be expressed with the transformation matrixes and DH-parameters. Coordinate change between two consecutive frames $i - 1$ and i can be formed with the following steps. Frame $i - 1$ is translated by d_i along z_{i-1} and rotated by an angle q_i about axis z_{i-1} . After this sequence, the frame $i - 1$ is aligned with frame i' and this can be presented by homogenous transformation matrix

$$A_i^{i-1} = \begin{bmatrix} \cos(q_i) & -\sin(q_i) & 0 & 0 \\ \sin(q_i) & \cos(q_i) & 0 & 0 \\ 0 & 0 & 1 & d_i \\ 0 & 0 & 0 & 1 \end{bmatrix}.$$

Next, the frame aligned with the frame i' is translated by a_i along the axis $x_{i'}$ and rotated by α_i about the axis $x_{i'}$. With these steps the frame i' is aligned with the frame i and the homogeneous transformation matrix is described as follows

$$A_i^{i'} = \begin{bmatrix} 1 & 0 & 0 & a_i \\ 0 & \cos(\alpha_i) & -\sin(\alpha_i) & 0 \\ 0 & \sin(\alpha_i) & \cos(\alpha_i) & 0 \\ 0 & 0 & 0 & 1 \end{bmatrix}.$$

The total coordinate transformation between the frames can be described with single matrix by multiplying matrixes above

$$A_i^{i-1} = \begin{bmatrix} \cos(q_i) & -\sin(q_i) \cos(\alpha_i) & \sin(q_i) \sin(\alpha_i) & a_i \cos(q_i) \\ \sin(q_i) & \cos(q_i) \cos(\alpha_i) & -\cos(q_i) \sin(\alpha_i) & a_i \sin(q_i) \\ 0 & \sin(\alpha_i) & \cos(\alpha_i) & d_i \\ 0 & 0 & 0 & 1 \end{bmatrix}. \quad (\text{A. 9})$$

The matrix formed by the first three rows and columns describe the orientation of the frame, and the first three rows of the last column describes the position of the frame. According to [67], the total transformation between the base frame and the end effector can be calculated by multiplying all the homogenous transformation matrices between individual frames. Equation below represents the transformation matrix of the mobile manipulator used in this thesis.

$$T_7^0 = A_2^1 A_3^2 A_4^3 A_5^4 A_6^5 A_7^6. \quad (\text{A. 10})$$

The expression for the mobile manipulator is very long therefore the matrix is not show here.

APPENDIX D: SIMULATION MODEL

Simulation model is modelled with MATLAB Simulink, and it consists of four different blocks. The first block, *Path generator*, makes a smooth path from given x- y- and z- coordinate vectors. The second block, *Jacobian and Forward Kinematics*, forms the reference for the joint angles. The third block, *Controller and EMLAs*, contains controllers, motors, and mechanical models for all EMLAs. Last block, *Simscape*, contains the multi-body model of the mobile manipulator. The top level of the model is shown in Figure F.

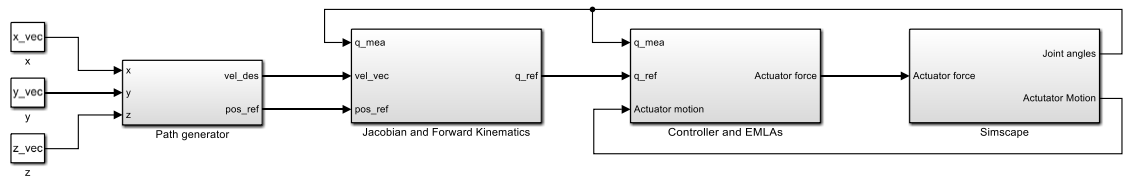


Figure F. Top level of the model.

Jacobian and Forward Kinematics block contains function for calculating the pseudoinverse Jacobian matrix and forward kinematics from the measured position of the joints. The MATLAB functions for calculating the forward kinematics and the pseudoinverse Jacobian are generated using MATLAB Symbolic Toolbox. The transformation matrix from base frame to end-effector are calculated with methods described in Appendix C. The block diagram of the Jacobian and inverse kinematics block is shown in Figure G.

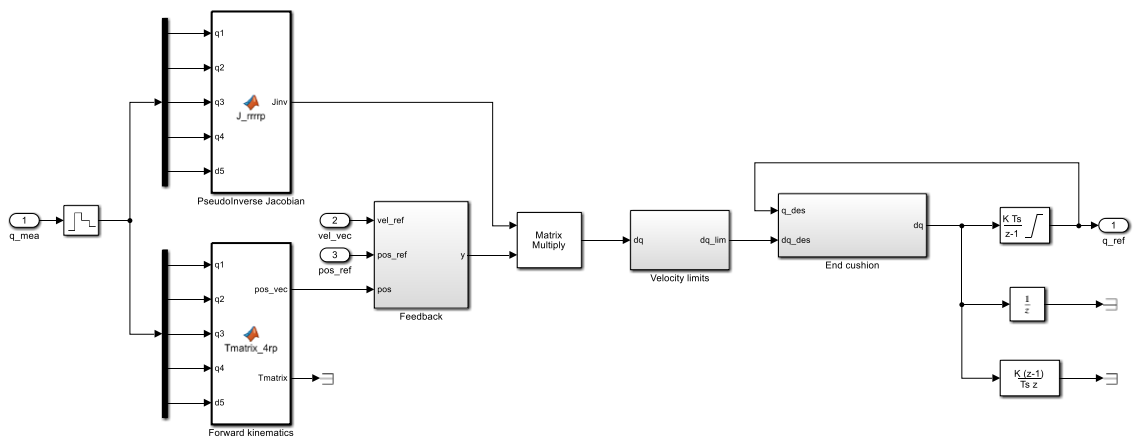


Figure G. Block for Jacobian and Inverse kinematics.

The joint velocity references from matrix multiplication of the pseudoinverse Jacobian matrix and tool center point (TCP) velocity vector are limited according to maximum actuator velocities. End cushion block decelerate the actuator near the motion limits to get

the impacts smoother. Next, the allowed velocities are integrated to position reference which is saturated according to joint limits. Further, the position reference goes to the controller including the position, the velocity and the current loop.

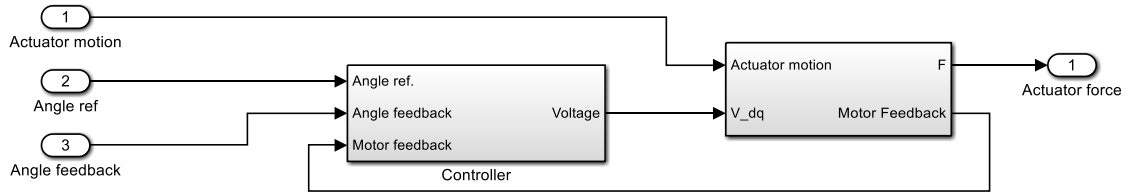


Figure H. A controller block and a block for a motor and mechanical model of single EMLA.

The inputs of the mechanical model are the motor velocity and the physical motion of the mobile manipulator. The mechanical model converts the rotational motion into the linear motion of the actuator according to the gear ratio of the gearbox and the lead of the ball screw. The model is shown in Figure I.

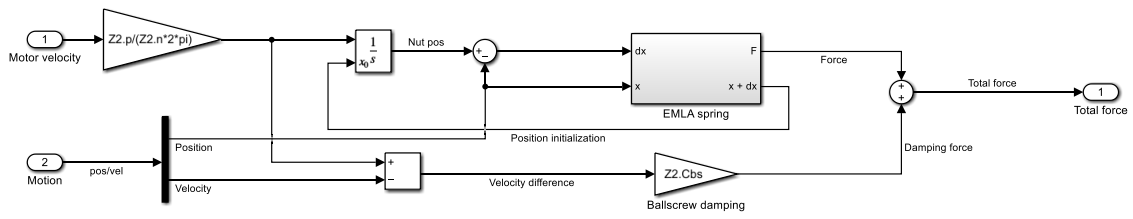


Figure I. The mechanical model of the second EMLA.

EMLAs can be modelled as a spring consisting of different stiffness components. The spring model shown in Figure J consist of stiffness components from the screw shaft, the screw nut, the thrust bearing and the rod of the actuator. The stiffness values for these components are calculated and obtained from manufacturer's datasheets.

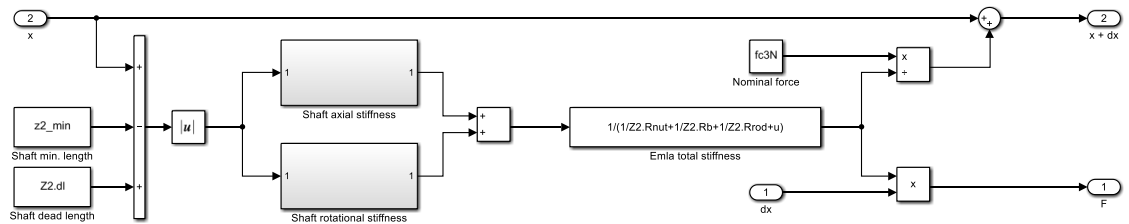


Figure J. The spring model of the second EMLA.

The spring model calculates the nominal position of the nut and the spring force generated by the position difference between the nominal length and the compressed length of the spring. This force is applied to the MATLAB Simscape Multibody model which calculates the motion of the manipulator and visualize it in Mechanics Explorer. The mobile manipulator is modelled with Solidworks and the Simscape Multibody model

is constructed with STEP-files from Solidworks. The model of the mobile manipulator is shown in Figure K.

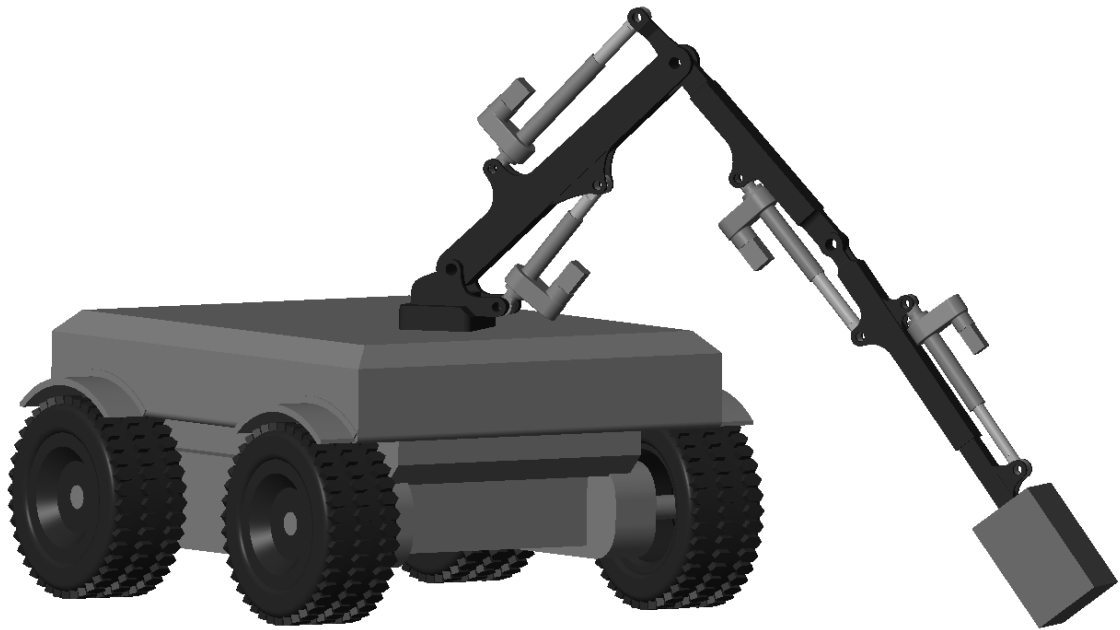


Figure K. *The MATLAB Simscape Multibody model.*

The inertia parameters of the mobile manipulator can be obtained from Solidworks, or they can be calculated using MATLAB's own feature which calculates the inertia of the components from the geometry. The box in the Figure K represent the load to be lifted.